US Army Corps of Engineers®
Engineer Research and Development Center

ERDC
ENGINEER RESEARCH & DEVELOPMENT CENTER

Installation Technology Transition Program (ITTP)

Initial Data Collection from a Fiber-Optic-Based Dam Seepage Monitoring and Detection System

Anna M. Wagner, Arthur B. Gelvin, Jon B. Maakestad, Thomas Coleman, Dan Forsland, Sam Johansson, Johan Sundin, and Chandler S. Engel

October 2023

Initial Data Collection from a Fiber-Optic-Based Dam Seepage Monitoring and Detection System

Anna M. Wagner, Arthur B. Gelvin, and Jon B. Maakestad

US Army Engineer Research and Development Center (ERDC)
Cold Regions Research and Engineering Laboratory (CRREL)
4070 9th Street
Fort Wainwright, AK 99703

Chandler S. Engel

US Army Engineer Research and Development Center (ERDC)
Cold Regions Research and Engineering Laboratory (CRREL)
72 Lyme Road
Hanover, NH 03755-1290

Thomas Coleman and Dan Forsland

Silixa LLC
3102 W Broadway Street
Missoula, MT 59808

Sam Johansson and Johan Sundin

HydroResearch AB
Stora Marknadsvägen 15, 12th floor
SE-183 34 Täby
Sweden

Final Report

Abstract

Visual inspection is the most used method to detect seepage at dams. Early detection can be difficult with this method, and use of appropriate real time monitoring could significantly increase the chances of recognizing possible failure. Seepages can be identified by analyzing changes in water and soil temperature. Optical fiber placed at the embankment's downstream toe has been proven to be an efficient means of detecting real time changes at short intervals over several kilometers. This study aims to demonstrate how temperatures measured using fiber optic distributed sensing can be used to monitor seepage at Moose Creek Dam, North Pole, Alaska. The fiber optic cable portion of the monitoring system is installed along a section of the embankment where sand boils have occurred. Though no flood event occurred during this monitoring period, routine pumping tests of nearby relief wells resulted in an increase of soil and water temperature (up to 13°C) along a 100 m section where sand boils were detected during the 2014 flood events. Measurements during a flood event are expected to provide a quantitative assessment of seepage and its rate.

Contents

Figures and Tables

Figures

Tables

Preface

This page intentionally left blank.

1   Introduction

The Association of State Dam Safety Officials report that internal erosion caused 46% of dam failures in the US between 1800 and 1986 (Bridle 2017). Internal erosion occurs when the water that seeps through the dam carries soil particles away from the embankment, leaving voids in the structure. Without intervention, this erosion may finally lead to failure of the dam. Consequently, early detection of internal erosion is of key importance to reduce risks and ensure the safety of dams. Many dams have limited or even no instrumentation to identify early signs of seepage.

1.1   Background

Verifying structural integrity and capacity of dams is challenging. The most common method of dam surveillance is through visual inspection (Johansson and Sjödahl 2004). Internal erosion is difficult to visually detect in early stages. Soil particles that are transported with the water flow may create sand boils indicating that the seepage gradient is sufficient to cause internal erosion, at least locally. However, the presence of sand boils is not a reliable early warning indicator, their formation is too variable to provide any meaningful predictions regarding potential dam failure timelines. To date, there is no reliable documentation linking sand boil formation and time to structural failure in dams.

Dam surveillance by visual inspection can yield early indicators of internal erosion by looking for signs of seepage. Evidence of internal erosion would be wet areas, increased internal drainage flow, surface erosion, and deformations such as cracks or sink holes. In cases where seepage is measurable with a weir or other devices, changes in the quantity of seepage flow can be carefully monitored. Unfortunately, seepage detection by visual means can only be accomplished in visible areas, movement of water in the internal structure of a dam must be detected by other means. The presence of subsurface seepage anomalies can be detected by monitoring changes in physical soil parameters such as pore pressure, temperature, self-potential, and resistivity (Bolève et al. 2007; Johansson 1997; Sjödahl et al. 2009). However, seepage could go undetected by conventional monitoring methods because of the sparse distribution of automated monitoring locations and the timing between scheduled inspections.

One of the most important physical parameters directly related to internal erosion is temperature. Measuring temperatures is one of the most sensitive methods for seepage flow detection (Johansson and Sjödahl 2004). Monitoring seepage in dams using temperature measurements was introduced in the late 1950s (Kappelmeyer 1957). During seepage there will be an increase in temperature that is driven by the influx of warmer surface water. An altered thermal distribution can be used to indicate water seepage (e.g., where a low temperature response indicates low seepage flow).

Traditional manual or automated temperature measurements in localized piezometers (i.e., standpipes) result in a coarse spatial resolution and a limited monitoring dataset of the embankment dam that may not be sufficient to detect potential water seepage. More recently, the ability to measure temperatures using distributed temperature sensing (DTS) with optical fibers has resulted in an opportunity for a continuous monitoring dataset along the total length of the embankment at high spatial and temporal resolutions. A continuous temperature dataset collected via fiber optic technology (Figure 1) has a higher probability to detect seepage anomalies in dam structures due to the spatio-temporally continuous covered provided by distributed sensing. Additionally, long-term, continuous temperature monitoring will increase the accuracy of seepage velocity estimation and lead to a better understanding of the thermal processes in the dam (Johansson and Sjödahl 2017). Finally, the use of fiber optic measurements provides for flexible application; for example, on installations where horizontal installation is impractical, fiber optic measurements in vertical piezometers (preferred horizontal distance of 10 m) is possible where several piezometers can be installed (Johansson and Sjödahl 2011).*

DTS was introduced in the late 1980s (Dakin et al. 1985; Kurashima et al. 1990) and has since resulted in an increase of using temperature measurements for internal erosion and seepage flow monitoring (Johansson and Sjödahl 2017). For the last three decades, integration of fiber optic cable in existing dams in Sweden has been the common practice (Johansson and Sjödahl 2017). Quinn et al. (2019) emphasizes how DTS

---

* For a full list of the spelled-out forms of the units of measure used in this document and their conversions, please refer to *US Government Publishing Office Style Manual*, 31st ed. (Washington, DC: US Government Publishing Office, 2016), 248–52 and 345–47, https://www.govinfo.gov/content/pkg/GPO-STYLEMANUAL-2016/pdf/GPO-STYLEMANUAL-2016.pdf.

can provide a higher spatial resolution monitoring system to detect seepage in under-documented dams.

The thermal monitoring method using fiber optical cable was recommended for seepage detection at dams by the International Commission on Large Dams (ICOLD) (Bridle 2017) ". . . Many less means of detecting seepage are now available. The most promising is temperature measurements which can be used to infer localized flow. Fiber optic cables facilitate data collection and make it possible to cover large parts of the dam."

Figure 1. Continuous temperature measurements using a fiber-optic monitoring system at a dam structure.
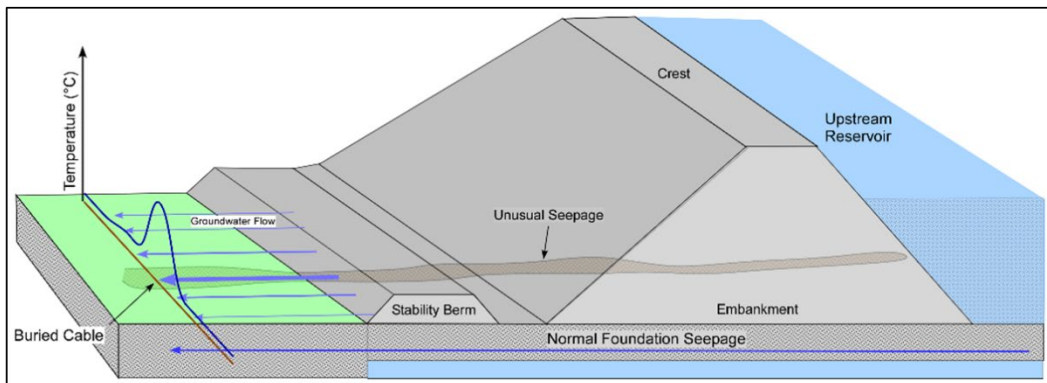
1.2 Objectives

The objective of this study is to demonstrate the use of fiber optic DTS to provide a reliable and comprehensive groundwater seepage monitoring system in dams at DoD installations. The proposed effort tests the reliability and feasibility of fiber optics as an automatic early warning system capable of detecting anomalies well before they are physically visible. This method of an early detection system for groundwater seepage is widely used in Europe and elsewhere in the world but has not yet been deployed at any US DoD installations. This study focuses on the installation of a fiber optic cable in the seepage zone downstream of an existing dam and measurement of temperature along this cable.

1.3 Approach

This effort includes deployment of a fiber optic cable and monitoring system at the US Army Corps of Engineers (USACE) Moose Creek Dam (MCD) Chena River Lakes Flood Control Project in North Pole, Alaska (Figure 2). This site was selected for a few reasons, including a recent and

growing automated piezometer-based monitoring system and previous dam seepage evidence. Thermal processes resulting from internal erosion can also be simulated by numerical modeling. Such simulations enable the comparison of an intact dam and a dam with significant seepage and leakage paths temperature fields which will help guide the interpretation of recorded data. Therefore, this effort also includes numerical modeling of both flood and no flood events at MCD.

Figure 2. Chena River Lakes Flood Control Project site location. (Images reproduced from Maxar©, Open StreetMap, and US Census Bureau.)
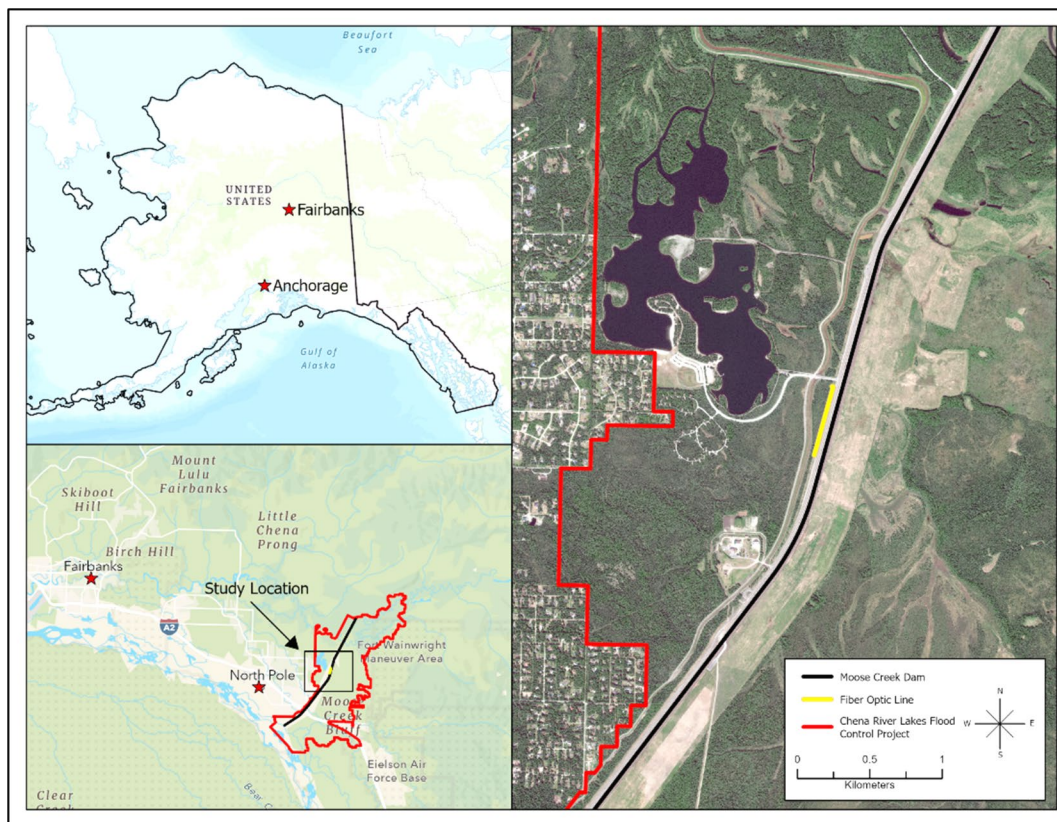
2   Methods

2.1   Site Description

The MCD is about 27 km east of Fairbanks, Alaska. The dam is a 12 km long and 15 m tall earthen structure that typically functions as a dry dam (Gelvin et al. 2019). However, the dam impounds and redirects water from the Chena River during periods of high-water levels caused by rapid snowmelt or heavy rains, providing flood control for the downstream communities of Fairbanks, North Pole, and Fort Wainwright. Nearly 1,400 small pin holes to large sand boils (up to about 3 m in diameter) were discovered in the summer 2014 after two minor flood events took place (USACE 2018). These were located downstream of the stability berm, mainly in an area of degraded permafrost (Figure 3). Because of this previous distress in this area, we chose this section of the dam for our fiber optic DTS site.

This part of the MCD (Sta 254+25 to 402+00) is founded on soil (Figure 4) consisting of various layers with highly permeable material. Drillings in the upper 30 m show mainly layers of sand and gravel. It is a zoned earth embankment, with a sloping core of semipervious (silty) gravel and shells of free-draining gravel. It has also relief to relieve the uplift pressures in the dam foundation during flood events. Relief well depths vary according to the extent of permafrost. There is also a 21 m wide downstream berm and a ditch invert 1.2 m below the berm. Culverts are placed each 2+00 between Sta 290+00 and 310+00 on Elevation +492. They are connected to the ditch invert. No blanket is used along this part of the dam and the dam height is about 7.6 m.

The current monitoring system at the MCD includes open-pipe piezometers, relief wells, weir staff gages and USGS river gages, groundwater wells and snowpack telemetry (SNOTEL) sites (maintained by the Natural Resource Conservation Service). During a flood event, the primary focus is on the pool elevations and water levels in the 144 piezometers, that are spaced far apart (150 m with closer spacing in areas of concern) along the 11+ km long dam embankment. The piezometer is used to measure groundwater levels at a specific point either manually (daily during operational events) or using automated groundwater level loggers. Currently, most of the piezometers are in locations that have not shown signs of seepage distress (USACE 2018). Piezometers are spaced

too far apart to serve as a seepage monitoring system for small, localized failures of the dam.

Figure 3. Close-up of the fiber optic line (*black line*) installation and current Moose Creek Dam (MCD) monitoring network. The location of 2014 sand boils are marked as areas of distress (*orange*). (Map reproduced from Maxar©.)
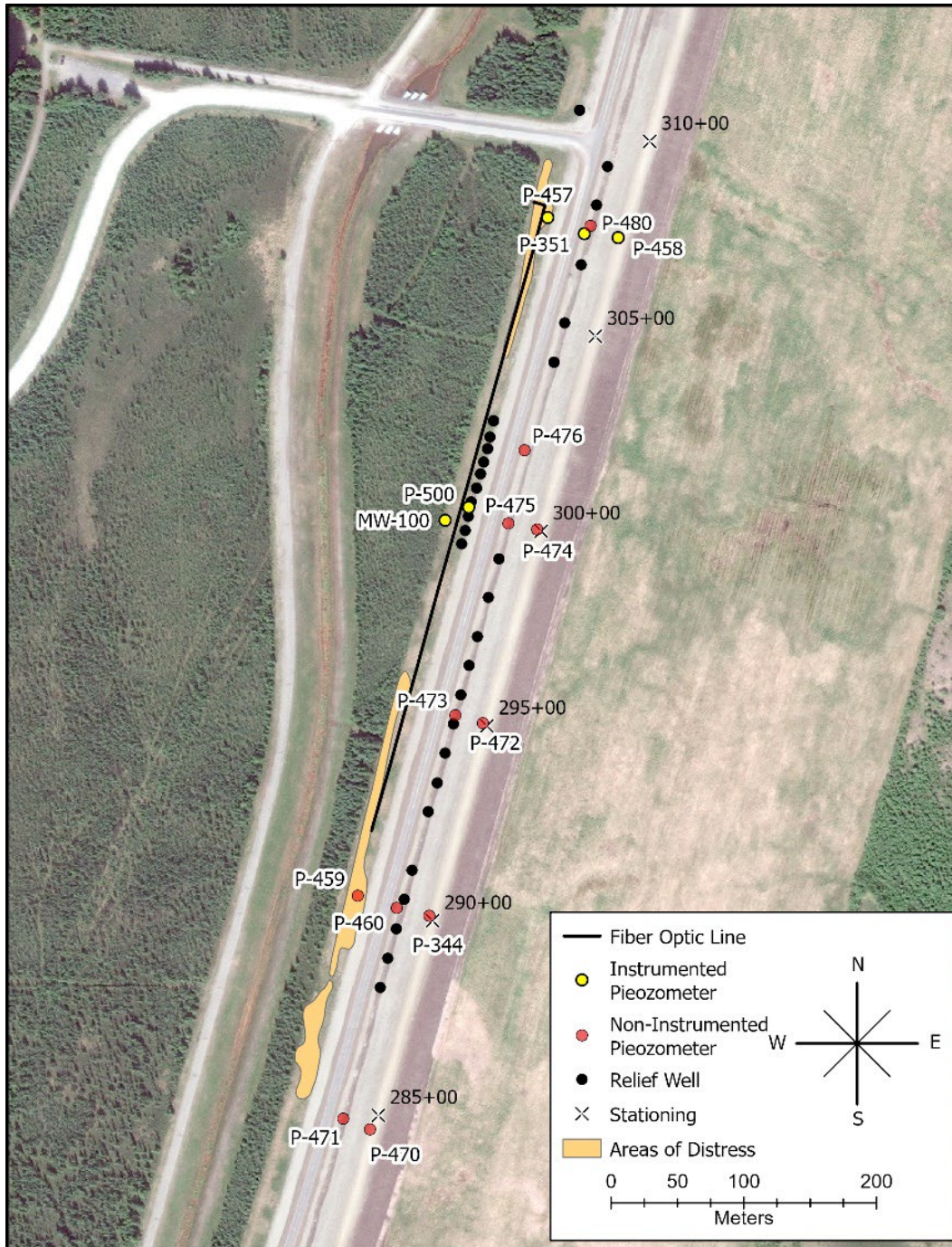
Figure 4. Cross section of the MCD, Station (Sta) 254+25 to 402+00. (Image reproduced from USACE 2016. Public domain.)
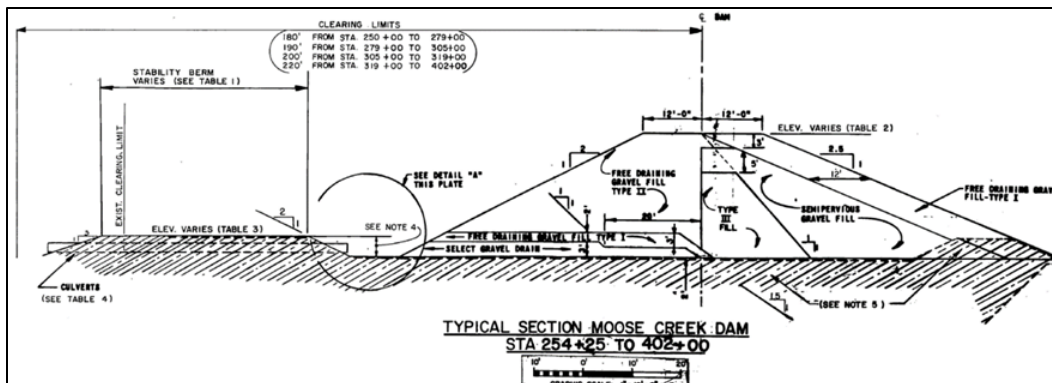
As a part of an on-going effort of the Alaska District to have real time monitoring of all the piezometers, and increasing the chance of identifying potential issues within the dam, Campbell Scientific (CS) electronic sensors (CS451, Campbell Scientific) have been placed in several piezometers along the MCD. From 2018 to 2022, 59 piezometers were equipped with sensors to monitor the liquid pressure of the column of water (the piezometric head) and the groundwater temperatures. Close to our study site, Station (Sta) 307+50 (station distances are in feet), sensors (CS451) were placed in three piezometers (P) wells (P-351, P-457, and P-458; Figure 5).

Figure 5. Placement of CS451 sensors in piezometer (P) wells (P-351, P-457, and P-458) at Sta 307+50.
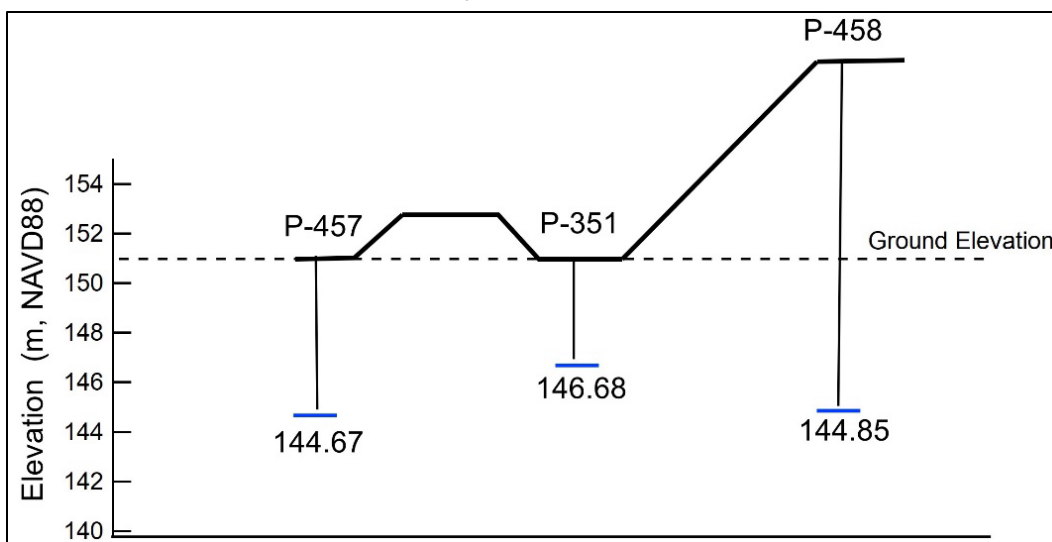
In addition to the hydrological monitoring at MCD, there is a meteorological station located at the USACE-Alaska District Chena project

office (latitude 64.76, longitude −147.22), about 1,000 m from the study site. Figure 6 shows the air temperature and precipitation for the 2022 summer. About midway, and 5 m west of the fiber optic cable, soil temperatures are continuously measured at every 0.3 m down from the ground surface to about 15 m (Monitoring Well [MW]-100, Figure 3).

In the summer of 2022, a USACE Alaska District contractor performed routine testing of relief wells (Figure 7) at the MCD. During that testing, water was pumped at several locations next to the fiber optic cable (Figure 8). The relief test dates, and Stations (in feet) are listed in the table embedded in Figure 7.

Figure 6. Air temperature (*blue*) and precipitation (*black*) at the MCD meteorological station.
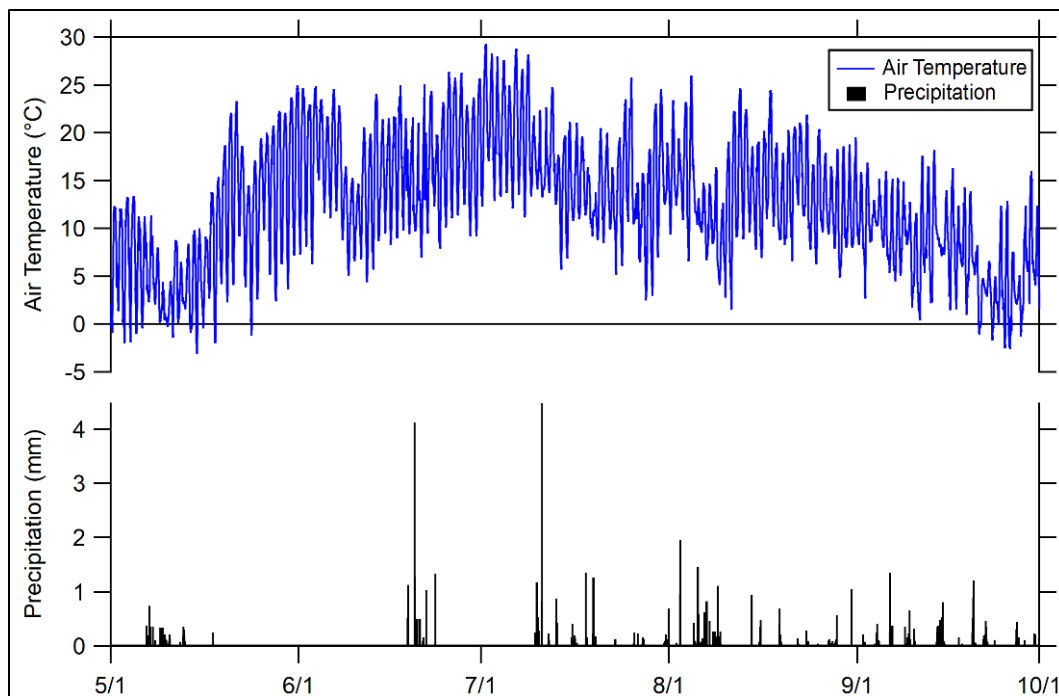
Figure 7. Relief well stations, and dates for relief well tests.

Date	Relief well stations
6/22	299+00, 299+15
6/23	297+00, 298+00
6/24	295+50, 296+25
6/25	294+00, 294+75, 309+00
6/27	292+50, 293+50
6/28	291+00
6/29	289+50, 290+25
6/30	288+00, 288+75, 306+50
7/1	304+00, 305+00, 308+00
7/6	299+85
7/7	299+50
7/12	300+20, 301+25
7/13	300+58, 301+60
7/14	300+90, 301+90, 302+30
7/26	299+15
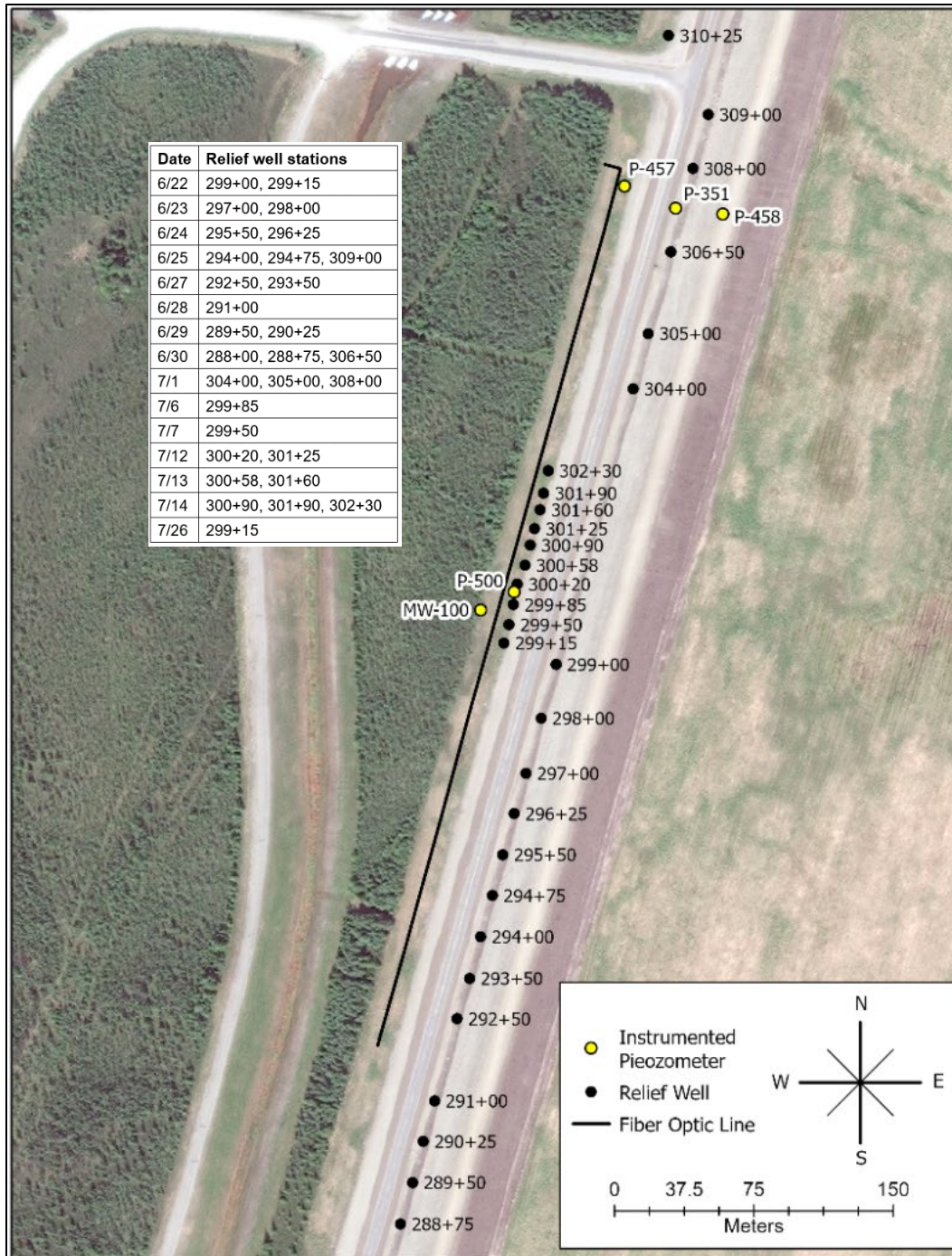
Figure 8. Two relief wells along the fiber optic line *(a)*, and movement of relief well flow conduit prior to installation of fiber optic cable *(b)*.
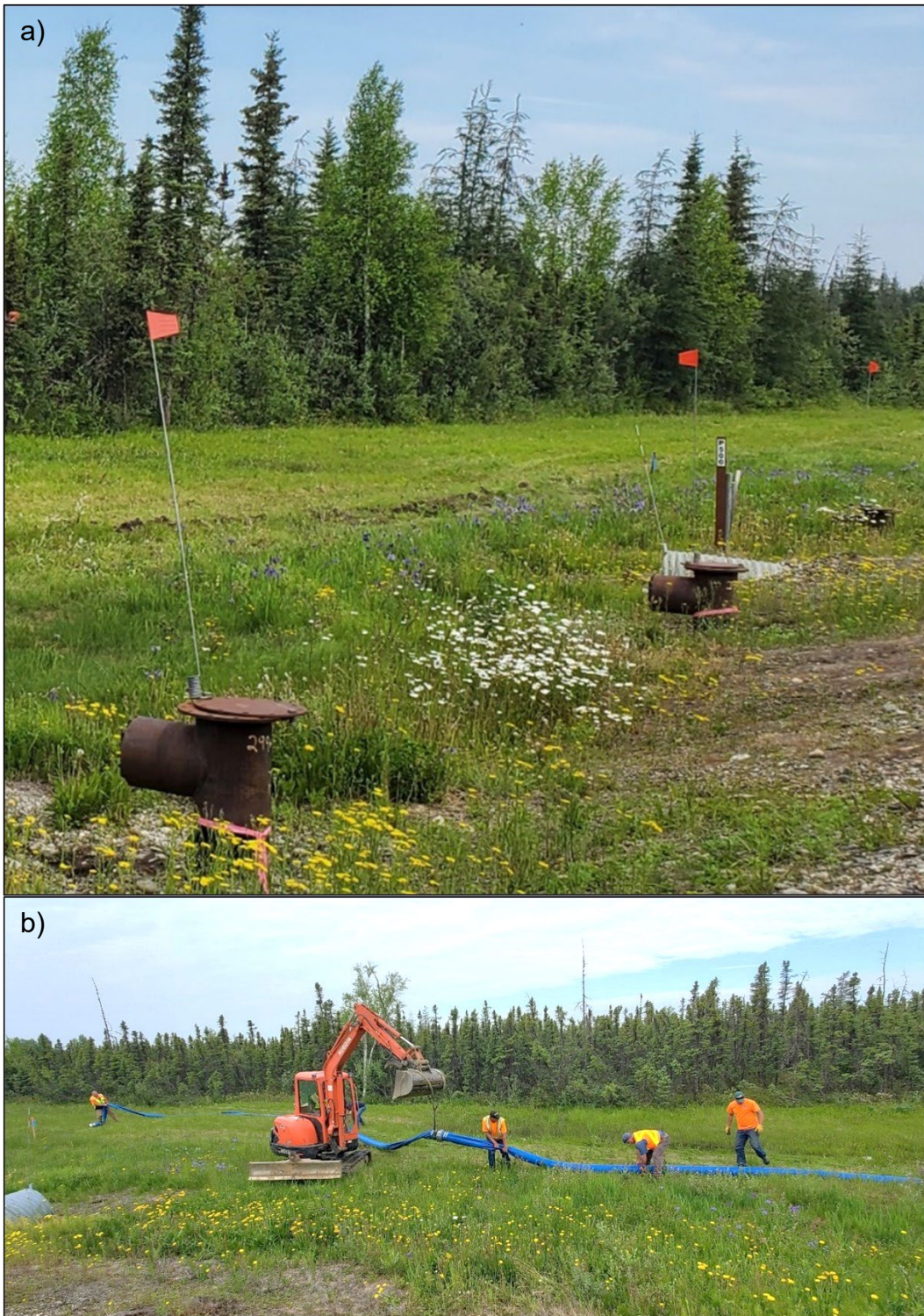
2.2 Fiber optic cable installation

On 22 June 2022, we installed a 500 m long tight-buffered direct bury fiber optic cable (Figure 3 and Figure 9) at a depth of about 2 m using a cable plow (Figure 10). The cable plow was a Bron 350 series, designed to install underground utilities at a depth of up to 198 cm. Cable plows utilize a slim profile blade to create a collapsing void space underground. As the plow is pulled through the soil, underground utilities are fed into the void space immediately behind the blade by means of a chute attached to the back of the blade. As the void space collapses, the underground utility and associate marking materials are securely held at a controllable depth from the surface. Some of the advantages to this installation method are its low impact to surrounding soils, speed of installation (depending on soil type), and high degree of depth control.

Figure 9. Direct-bury cable with 4 multimode (MM) and 2 single mode (SM) optical fibers.
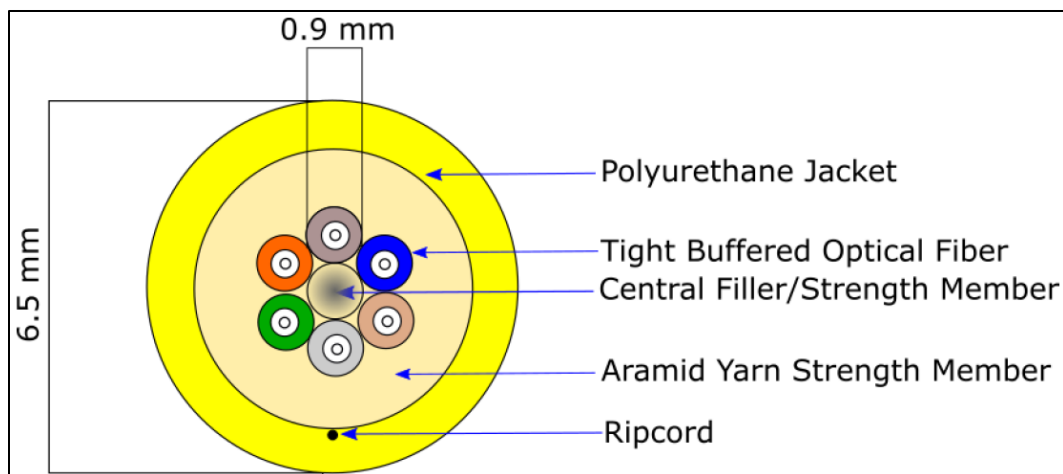
Figure 10. Fiber optic installation with a cable plow.

The fiber optic line paralleled the earthen dam, offset from the toe by 40 m (Figure 11), and it included both a control section, and a section known for the occurrence of sand boils (Figure 3). By installing the cable at depth, we were able to install above groundwater elevations during flood events, this allowed the greatest chance to capture ground temperature fluctuations driven by dam seepage as warmer surface water was drawn into the groundwater table.

Prior to the installation of the fiber optic cable, the cable plow made one pass along the 500 m long distance (from north to south; piezometer P-457 and past piezometer P-473, Figure 3) as a preparatory step before cable installation (Figure 10). At the end of the fiber optic line (south end), the fiber optic cable was spliced into a splicing box that was buried in an approximately 1 m by 4 m soil pit excavated by a small excavator (Figure 12) as a starting point (end point for monitoring) for the fiber optic cable.

Once preparations were complete, fiber optic cable, marking tape, and locator tape were fed into the cable plow chute and the plow was lowered into the soil pit where the second pass with the cable plot completed the installation (Figure 12) This method of installation proved to be very time-efficient, after preparations were made, the entire 500 m section of cable was seated at depth in under an hour.

Figure 11. MCD embankment profile.
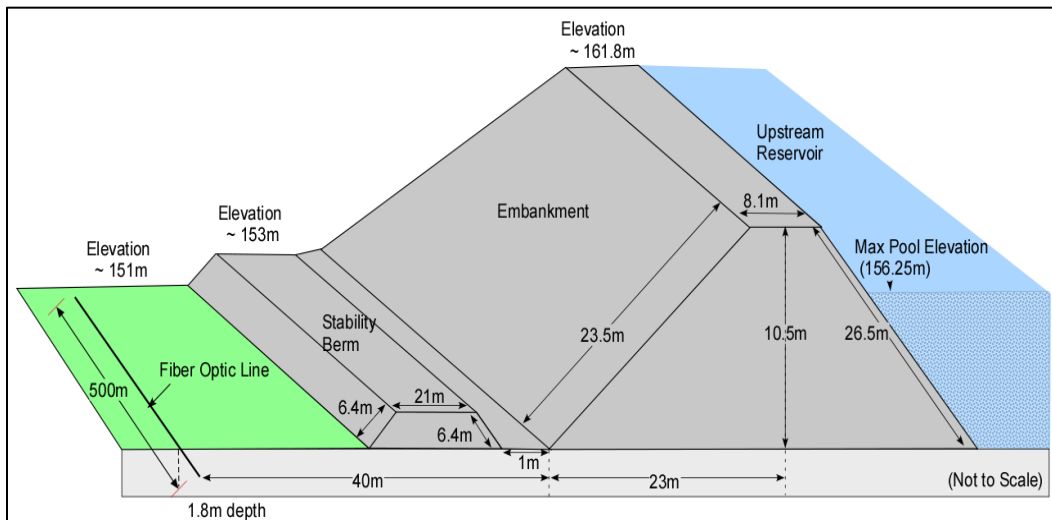
Figure 12. Soil pit at the south end of the fiber optic line.

2.3 Distributed Temperature Sensing (DTS)

DTS uses Raman scattering to determine temperature (Tyler et al. 2009). A short laser pulse (<10 ns) is sent into an optical fiber and, as the light travels along the cable, the reflected light properties vary with temperature (Dakin et al. 1985; Tyler et al. 2009). This method provides a temperature profile distributed along the entire optical fiber. The sampling interval and temperature accuracy and resolution depend on the instrument, the type of optical fiber, and the total length of the fiber optic cable. For example, a 10 km long cable typical sampling interval is about 0.25 m with a temperature resolution of ±0.01°C (Johansson and Sjödahl 2017).

2.3.1 Setup of temperature monitoring unit

For this installation, we collected temperature measurements using a Silixa ruggedized DTS, XT-DTS. This unit is a low powered system designed for remote locations. We powered the unit using four, 12 V 100 Ah deep cell batteries configured to provide 24 V power to the instrument. Initially the system was energized utilizing two 50 W solar panels, but those proved to be insufficient for operation (Figure 13). The solar array was later expanded to a 4 panel, 200 W total configuration. To protect the unit from extreme environment, we installed the unit inside a customized enclosure specifically designed for the XT-DTS.

Continuous measurements were setup on a double ended configuration (Figure 14) for 15 min on channels 1 and 2 with no idle time between measurements (Channels 3 and 4 are not in use). The acquisition time was later reduced to 7.5 min per channel. Temperature offset correction was set up using the PT100 probe and reference section supplied within the enclosure.

Figure 13. Distributed temperature sensing (DTS) monitoring site and installation.

Figure 14. Configuration of optical fibers. *Green rectangles* represent E2000 connectors, *black solid dots* represent splices.
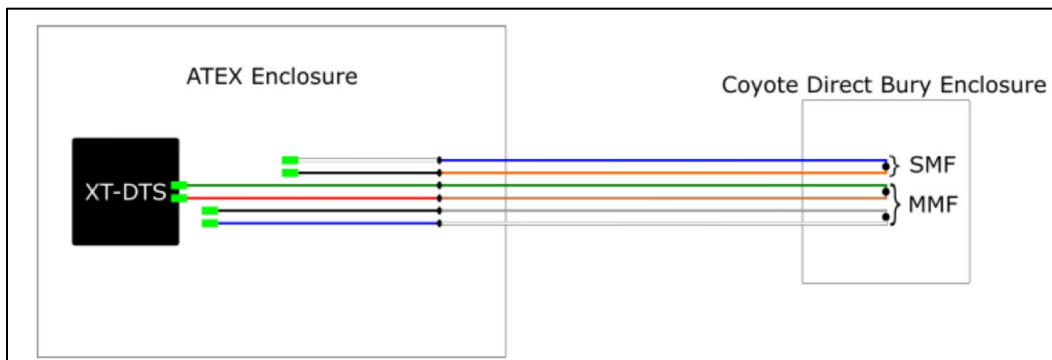
2.3.2 Cable coordinates and length calibration

The total measured length in one loop is 1,088 m. Measurements of the signal strength show excellent splicing of the fiber optic cable (Figure 15). The symmetry point (at 543.6 m) is clearly seen in the temperature data but hardly visible in the signal data.

Figure 15. Signal strength *(a)*, and temperature data along the entire fiber loop *(b)*.
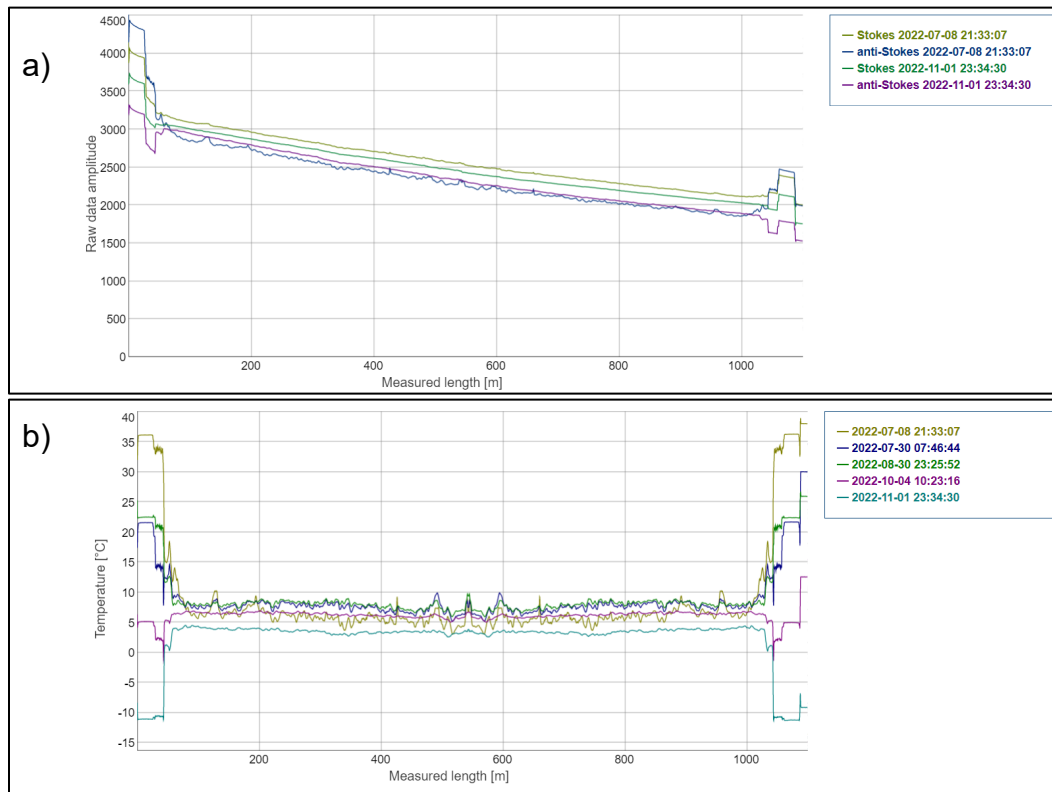
Cable coordinates and the length markings along the dam line (such as Sta 300+00) are indicated in Figure 16 and Table 1. Based on this information, together with the temperature data along the measured length, it is possible to link the temperature measurements to the dam line. Compensation for additional fiber length compared to the cable length is also necessary. The fiber is normally about 0.5% longer than the cable.

The temperature measurements indicate the interval where the cable is around its nominal depth. At this depth, temporal temperature variations are minor. Data in Figure 17 suggests 45 m as the interval's starting point and 537 m as the end point. It equals an effective length of 492 m (1614.2 ft). The cable length is slightly shorter. From Figure 17, we can estimate the Station for the starting point to Sta 307+85 and the endpoint to Sta

291+80. This gives a length of 489 m (1,605 ft). The length correction that matches these data is 0.55%, which seems reasonable. However, it should be noted that the estimations from the figure are probably more inaccurate than the corresponding measured data. The given data and the calculations are shown in Table 1.

Figure 16. Given cable points (Fiber-000–Fiber-016) shown as *blue circles* plotted on the fiber optic line (*red line*).
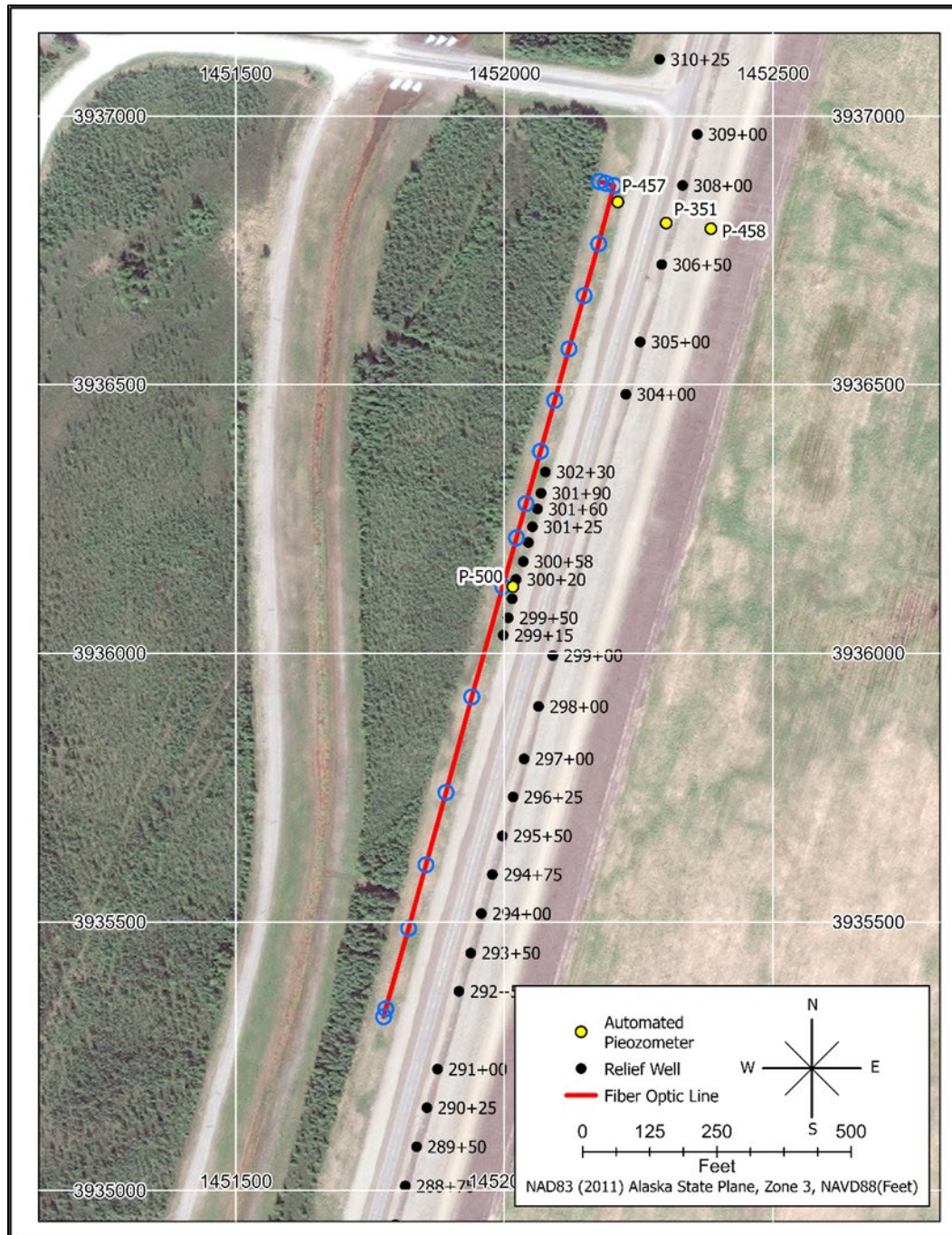
Table 1. Provided data (*left*) and calculated data (*right*). The *blue* and *yellow* fields are where the temperature data can be used for evaluation (between Stations [Sta] 291+80 and Sta 307+85). The *dark yellow* fields are the start and end data points of which the interpolation of fiber distance was made. Coordinate system is NAD83 (2011) Alaska State Plane, Zone 3, NAVD88 (feet).

Provided data					Calculated and matched data					
ID	Northing	Easting	Elevation (ft)	Comment	Distance (ft)	Sta from map	Fiber distance (ft)	Fiber distance (ft)	Fiber station (m)	Comment
—	—	—	—	DTS	—	—	Length corr	—	0	—
—	—	—	—	Pigtail loop	—	—	0.55%	—	26	—
Fiber-000	3936878	1452177	494.257	Control box	—	—		—	—	—
					12.6	—	—	—	—	—
Fiber-001	3936875	1452189	494.157	Trench	—	—	—	—	—	—
					16.2	—	—	—	—	—
Fiber-002	3936871	1452204	494.202	Trench	—	307+85	147.6	147.6	45	From data
—	—	—	—	—	112.1	—	—	—	—	—
Fiber-003	3936762	1452176	494.034	Trench	—	306+73	260.4	—	—	—
—	—	—	—	—	100.0	—	—	—	—	—
Fiber-004	3936666	1452149	495.049	Trench	—	305+73	361.0	—	—	—
—	—	—	—	—	103.1	—	—	—	—	—
Fiber-005	3936567	1452120	495.353	Trench	—	304+70	464.6	—	—	—
—	—	—	—	—	99.6	—	—	—	—	—
Fiber-006	3936471	1452094	495.341	Trench		303+70	564.7	—	—	—
—	—	—	—	—	98.2	—	—	—	—	—
Fiber-007	3936376	1452068	494.962	Trench	—	302+72	663.5	—	—	—
—	—	—	—	—	101.2	—	—	—	—	—
Fiber-008	3936279	1452040	495.391	Trench	—	301+71	765.2	—	—	—

Table 1 (cont.). Provided data (*left*) and calculated data (*right*). The *blue* and *yellow* fields are where the temperature data can be used for evaluation (between Stations [Sta] 291+80 and Sta 307+85). The *dark yellow* fields are the start and end data points of which the interpolation of fiber distance was made. Coordinate system is NAD83 (2011) Alaska State Plane, Zone 3, NAVD88 (feet).

Provided data					Calculated and matched data					
ID	Northing	Easting	Elevation (ft)	Comment	Distance (ft)	Sta from map	Fiber distance (ft)	Fiber distance (ft)	Fiber station (m)	Comment
—	—	—	—	—	66.0	—	—	—	—	—
Fiber-009	3936215	1452023	495.734	Trench	—	301+05	831.6	—	—	—
—	—	—	—	—	94.2	—	—	—	—	—
Fiber-010	3936124	1451997	495.682	Trench	—	300+11	926.3	—	—	—
—	—	—	—	—	213.5	—	—	—	—	—
Fiber-011	3935919	1451939	495.252	Trench	—	297+97	1140.9	—	—	—
—	—	—	—	—	184.1	—	—	—	—	—
Fiber-012	3935741	1451891	494.823	Trench	—	296+13	1326.1	—	—	—
—	—	—	—	—	139.9		—	—	—	—
Fiber-013	3935606	1451854	494.812	Trench	—	294+73	1466.7	—	—	—
—	—	—	—	—	122.7	—	—	—	—	—
Fiber-014	3935488	1451822	494.098	Trench	—	293+50	1590.1	—	—	—
—	—	—	—	—	170.8	—	—	—	—	—
Fiber-015	3935324	1451775	494.913	Trench		291+80	1761.8	1761.8	537	From data
—	—	—	—	—	—	—	—	—	—	—
Fiber-016	3935338	1451779	490.499	Fiber at depth	—	—	—	—	—	—
—	—	—	—	Total:	1605.3	1605.0	1614.2	1614.2	492	—

Figure 17. Estimated starting *(a)* and end points *(b)* where the cable is at the desired depth.
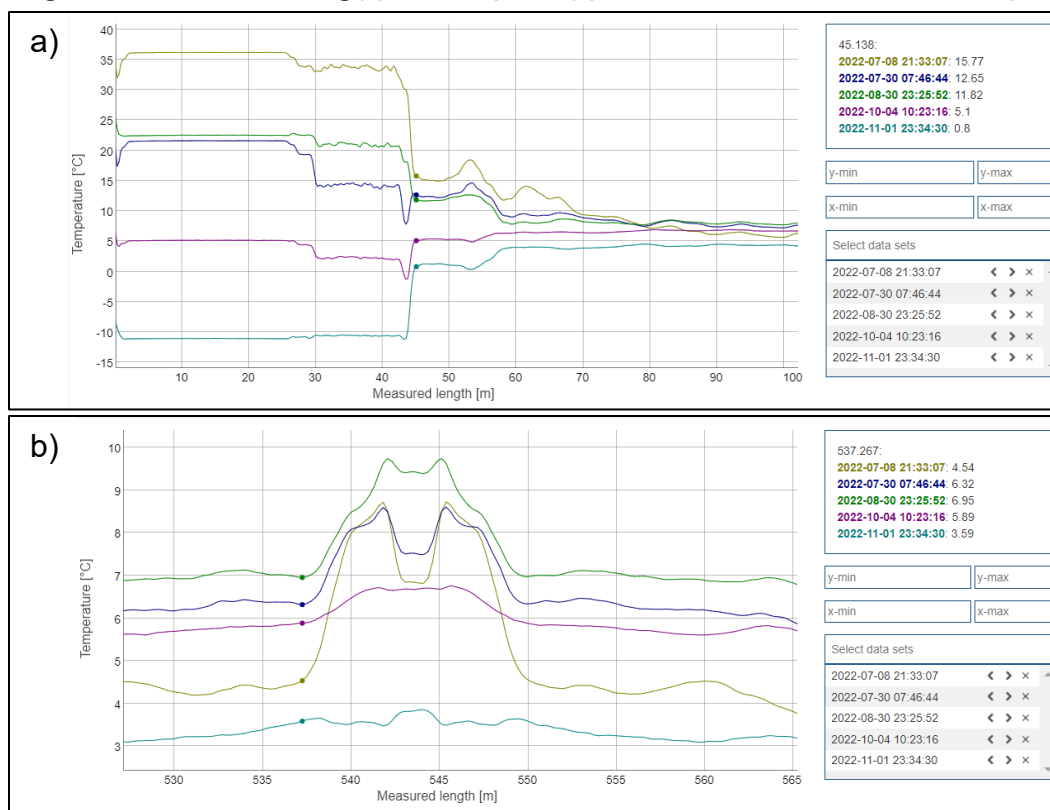
2.4   Numerical modeling of soil temperature

During this effort and time of installation, our fiber optic cable installation depth was limited by equipment availability in Alaska. Even though this was the limitation during this install, we performed preliminary simulations using the commercial multi-physics finite element modeling software COMSOL Multiphysics®. COMSOL Multiphysics is a registered trademark of COMSOL AB. The pressure and flow fields were computed with Richards' equation and the temperature by a heat transfer equation. Both two and three-dimensional (2D and 3D, respectively) simulations have been performed. Snow has not been accounted for, but frozen material was included in the 2D simulations.

2.4.1   Geometry and mesh

The 2D simulation geometry (Figure 18) was constructed based on a typical section between Sta 254+25 and 402+00 (Figure 4), the given embankment profile (Figure 1), and the geometry used previously for groundwater hydraulic modeling by USACE (2016). The 3D dam model

was constructed by extruding the 2D model 15 m. The streamwise, vertical, and dam station coordinates are x, y, and z, respectively.

The mesh was constructed from triangular or tetrahedral elements for the 2D (Figure 19) or 3D geometries, respectively. The maximum element size was set to 1 m except in the bottom foundation gravel (and sand) layer. There, the maximum element size was 2 m. The number of elements of the 2D and 3D grids were 12,000 and 680,000, respectively. One simulation scenario was repeated with different grids to show that the results were independent of the mesh to a satisfactory degree (Section 3.3.2).

Figure 18. The 2D geometry used in the COMSOL Multiphysics® simulations. The colors correspond to the different materials.
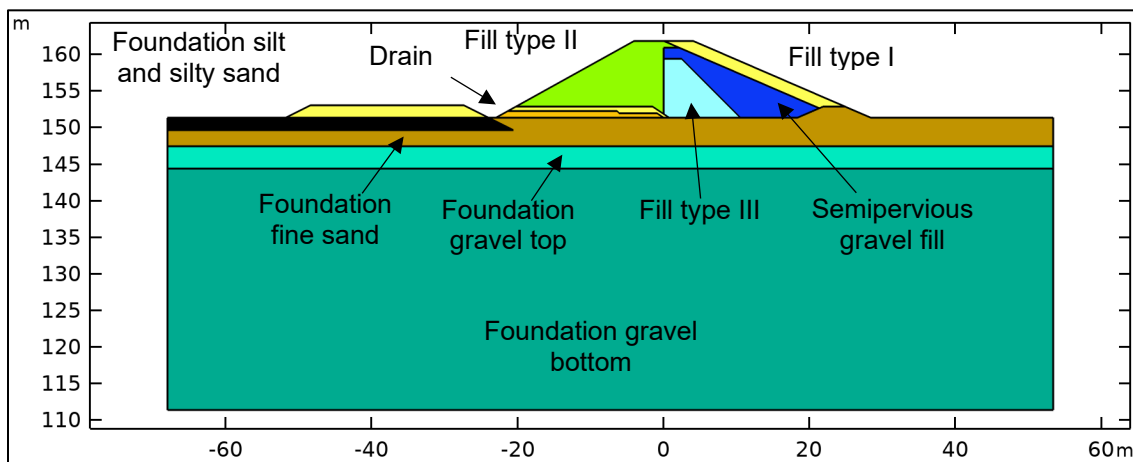
Figure 19. The 2D simulation mesh.
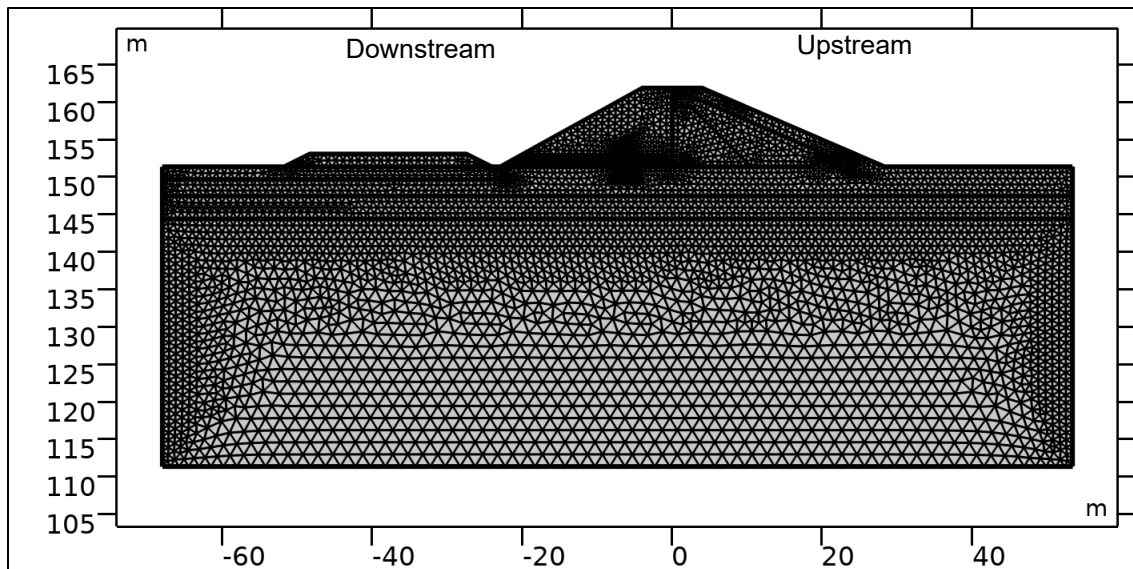
2.4.2 Material properties

Nine different solid materials were considered (Figure 18 and Table 2). Permeabilities correspond to values used by USACE (2016). Table 3 lists water (unfrozen and frozen) and air properties applied in the model. The 3D model requires the permeability to be specified also in the z-direction. Due to the typically low velocity in this direction, this parameter is of minor importance. It was set equal to the permeability in the x-direction.

Table 2. Solid porous matrix parameters.

Parameter		Unit	Fill type I	Fill type II	Fill type III	Drain	Semiperv. gravel fill	Foundation silt	Foundation fine sand	Foundation gravel top	Foundation gravel bottom
Porosity	φ		3.50E-01	3.50E-01	2.50E-01	3.50E-01	3.50E-01	2.50E-01	2.50E-01	2.50E-01	2.50E-01
Permeability, x-dir.	$\kappa_{s,x}$	m^2	9.38E-11	4.70E-11	2.82E-11	9.38E-10	9.38E-12	1.17E-12	4.06E-11	4.70E-10	4.70E-10
Permeability, y-dir.	$\kappa_{s,y}$	m^2	7.51E-11	3.76E-11	2.25E-11	9.38E-10	7.51E-12	2.93E-13	1.02E-11	4.70E-10	5.17E-11
Porous matrix compressibility	χ_p	1/Pa	1.00E-08	1.00E-08	1.00E-08	1.00E-08	1.00E-08	1.00E-08	1.00E-08	1.00E-08	1.00E-08
Inverse length scale	α	1/m	1.00E+00	1.00E+00	1.00E+00	1.00E+00	1.00E+00	1.00E+00	1.00E+00	1.00E+00	1.00E+00
Constitutive param. 1	n		2.00E+00	2.00E+00	2.00E+00	2.00E+00	2.00E+00	2.00E+00	2.00E+00	2.00E+00	2.00E+00
Constitutive param. 2	l		5.00E-01	5.00E-01	5.00E-01	5.00E-01	5.00E-01	5.00E-01	5.00E-01	5.00E-01	5.00E-01
Density	ρ_s	kg/m^3	2.70E+03	2.70E+03	2.70E+03	2.70E+03	2.70E+03	2.70E+03	2.70E+03	2.70E+03	2.70E+03
Specific heat capacity	$c_{p,s}$	J/(kg·K)	8.08E+02	8.08E+02	8.08E+02	8.08E+02	8.08E+02	8.08E+02	8.08E+02	8.08E+02	8.08E+02
Thermal conductivity	k_s	W/(m·K)	2.10E+00	2.10E+00	2.10E+00	2.10E+00	2.10E+00	2.10E+00	2.10E+00	2.10E+00	2.10E+00

Table 3. Water and air properties. (*Inco.* means *incompressible*.)

Parameter	Unit	Liquid water	Solid water (ice)	Air
Density	kg/m^3	1.00E+03 ($\rho_{w,l}$)	1.00E+03 ($\rho_{w,s}$)	1.25E+01 (ρ_a)
Specific heat capacity	J/(kg·K)	4.18E+03 ($c_{p,w,l}$)	2.10E+03 ($c_{p,w,s}$)	1.00E+03 ($c_{p,a}$)
Thermal conductivity	W/(m·K)	6.00E-01 ($k_{w,l}$)	2.10E+00 ($k_{w,s}$)	2.50E-02 (k_a)

Residual volume fraction	$\vartheta_{res} = 0$
Transition temperature	$T_{pc} = 0°C$
Transition interval width	$\Delta T = 10°C$
Latent heat	$L = 333$ kJ/kg
Water compressibility	$\chi_w = 0$ 1/Pa (inco.)

To simulate internal erosion, we assigned a region with highly permeable material into the 3D model. It extended from the upstream to the downstream side of the model. This region may also represent local/natural heterogeneities. Its porosity was 0.35 and the permeability 4.7×10^{-9} m² (10 times the permeability of the foundation gravel top layer, Table 2). The area of potential failure, or the defect's yz-plane cross-section was circular with a radius of 2 m.

In the 2D model, the flow and heat transfer equations were coupled since the dynamic water viscosity was assumed to depend on the temperature. Therefore, the viscosity is not given in Table 3, but shown in Figure 20. Freezing was modeled as a release of energy (the latent heat, L) around 0°C (using the apparent heat capacity method). The thermal conductivity and specific heat capacity of water also changed during the phase transition (Table 3). The density was kept constant for simplicity. In Richards' equation, the ice was modeled as fluid, however, with large

viscosity. Thus, around, and below 0°C (273 K) in Figure 20, the viscosity increases steeply with decreasing temperature. For material temperatures below −4°C, the dynamic viscosity was set to 0.05 Pa × s.

Since 3D simulations require more computational resources compared to a 2D model, the equations utilized in the 3D model were simplified. The Richards and heat transfer equations were solved separately, assuming a constant dynamic viscosity of 0.0015 Pa × s (corresponding to 5°C). Freezing was also neglected in the 3D simulations.

Figure 20. Dynamic water viscosity as a function of temperature.
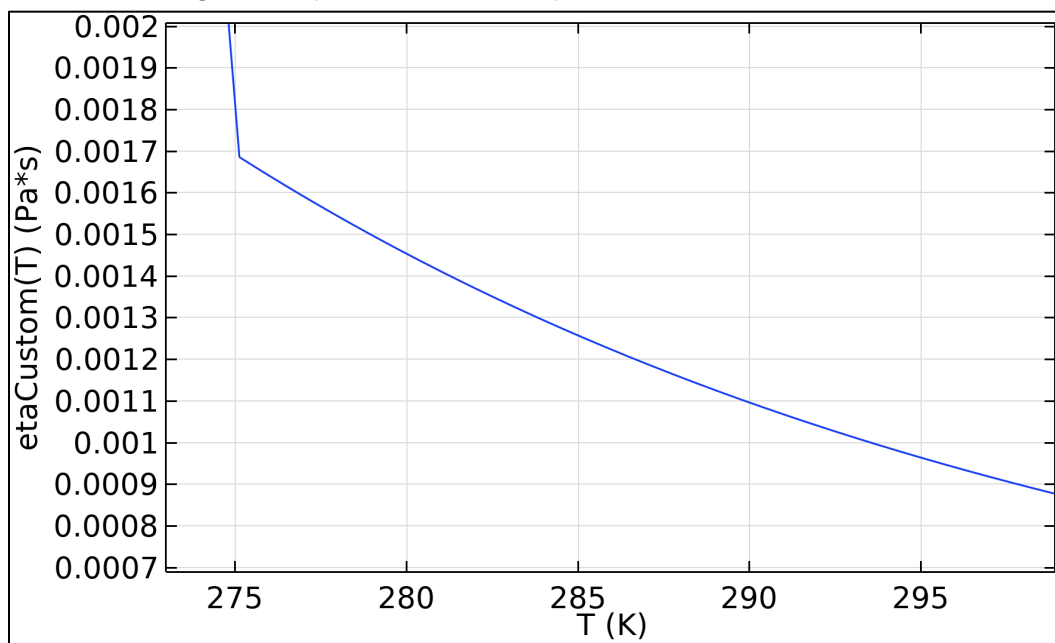
2.4.3 Boundary and initial conditions

Water table levels were specified upstream and downstream of the embankment. For Richards' equation, the boundary pressure was set equal to hydrostatic pressure below the water table (i.e., linearly increasing with elevation). Remaining boundaries had zero wall-normal flow (i.e., being impermeable, including the bottom side of the model). For the 3D model, this includes the boundaries in the z-direction. Zero wall-normal flow in the z-direction corresponds to a symmetry condition. In simulations with intermediate upstream water table levels, the transition between the hydrostatic pressure and the zero wall-normal flow conditions on the upstream side was imposed using the pervious layer boundary condition.

The downstream ground water level was set to +148.8 m. The ground water slope, during no flooding, was estimated from a ground water contour map published in USACE (2016) to $5/2000 = 2.5 \times 10^{-3}$. The numerical model is 121.4 m long, resulting in an upstream water level of +149.1 m. In the 2D simulation with high reservoir, the upstream water table was set to +160.5 m, similarly to the level used by USACE (2016).

In the 2D flooding simulation, the upstream water table level changed with time, according to Figure 21. It corresponds to a rising and decreasing water level in June and July, respectively. In the 3D flooding simulations, steady water levels corresponding to the lowest and highest levels of Figure 21 were imposed instead of a dynamically changing one (switching at the end of May).

Figure 21. Upstream water table level for one year.
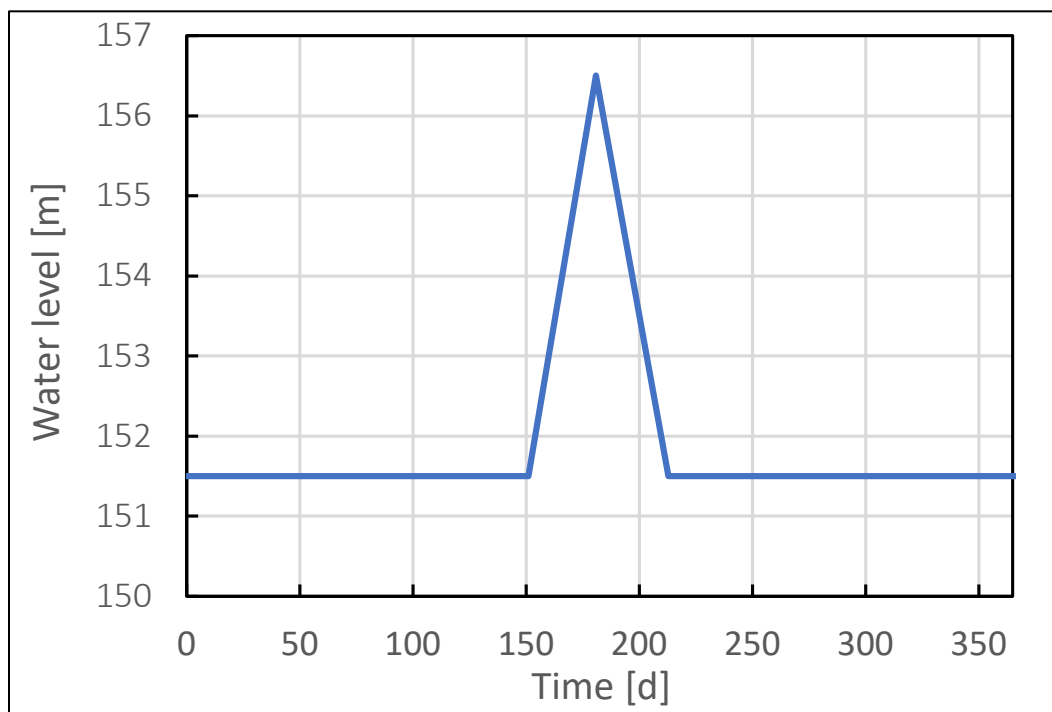
In the no flood 2D simulation, a ground water inflow temperature of 2°C was imposed. In the other simulations, a varying water temperature was set (from existing reservoir bottom to the water table). The remaining upstream side (below the water table) was assumed thermally insulated (e.g., zero wall-normal heat conduction). This combination of boundary conditions represents reservoir water that warms up during summer and a ground water temperature that is regulated by the reservoir. In all simulations, an air temperature was applied on the remaining boundaries

above ground. The ground water (for no flooding), reservoir, and air temperatures are shown in Figure 22. Remaining boundaries were thermally insulated.

When the pervious layer boundary condition was used for Richards' equation, a smooth transition between water and air temperatures was set over a vertical interval of ±1 m. In the 3D model, the thermal insulation was also imposed on boundaries in the z-direction, being equal to a symmetry condition.

The simulations were initialized using a steady flow solution and temperatures of 2°C. The time step was restricted to be less than or equal to 24 h except for the 2D high reservoir level and flooding simulations, where the limit was 8 h. The total simulation time for all models were five years (1,825 days). In the 3D simulations, the upstream water level change was only implemented in the last year.

Figure 22. Imposed groundwater or water reservoir temperatures (for no flood event or high reservoir level and flooding, respectively) as well as air temperatures for one year.
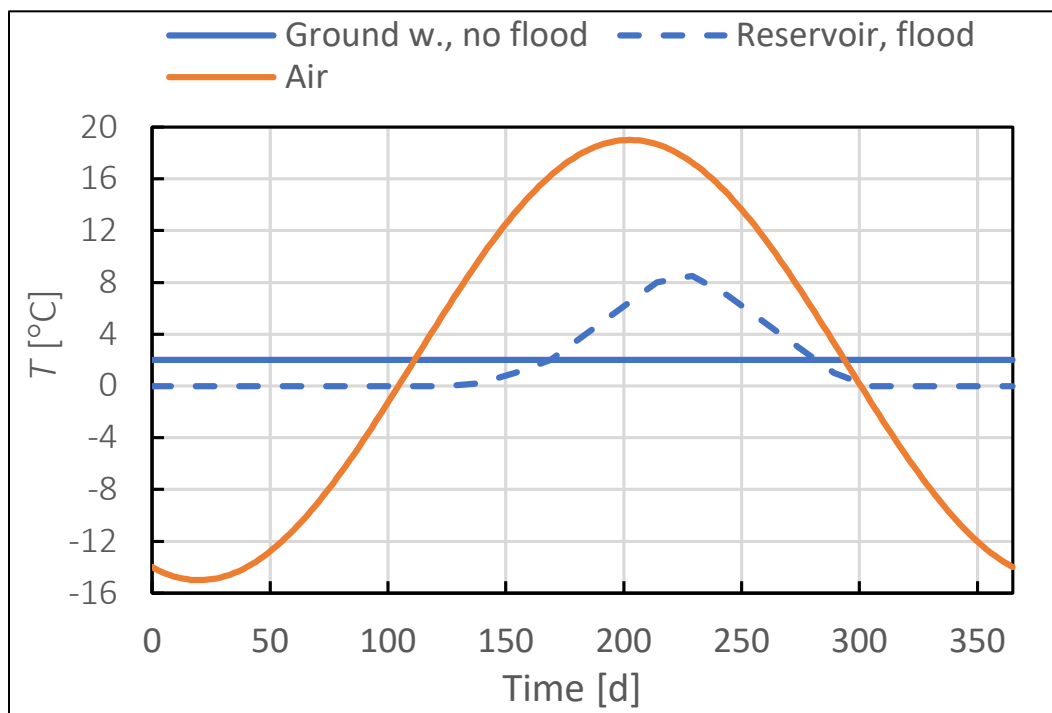
3   Results

3.1   Moose Creek Dam (MCD) Flood Project Monitoring

3.1.1   Groundwater Elevation Measurements

In 2022, groundwater elevations at MCD were monitored in
144 piezometers. At the piezometer cluster closest to the fiber optic cable,
groundwater elevations have been measured continuously with electronic
sensors beginning the summer of 2018 (Figure 23). Since 2018, the yearly
maximum groundwater elevations at this location varied about 2 m
(149.1 to 151.0 m) where the highest measured elevation was May 2020.
During that year, the MCD was in flood control status. In fact, the
groundwater elevation of 151.0 m was slightly above the ground surface
at this location (150.97 m), where the water level within the piezometer
was higher than the ground surface due to the hydraulic pressure of the
ground water. Additionally, during spring melt in 2022 (prior to the fiber
optic cable installation), the dam was close to flood status with the
elevation of the Chena River approximately 151.2 m. Operation of the
dam does not occur until the flow rate of the river reaches within
215 m³/s at the control works, and 340 m³/s (commonly closer to
297 m³/s–311 m³/s) at the downtown Fairbanks Chena River
USGS 15514000 gage.

Figure 23. Groundwater elevations at P-457 (*black line*).
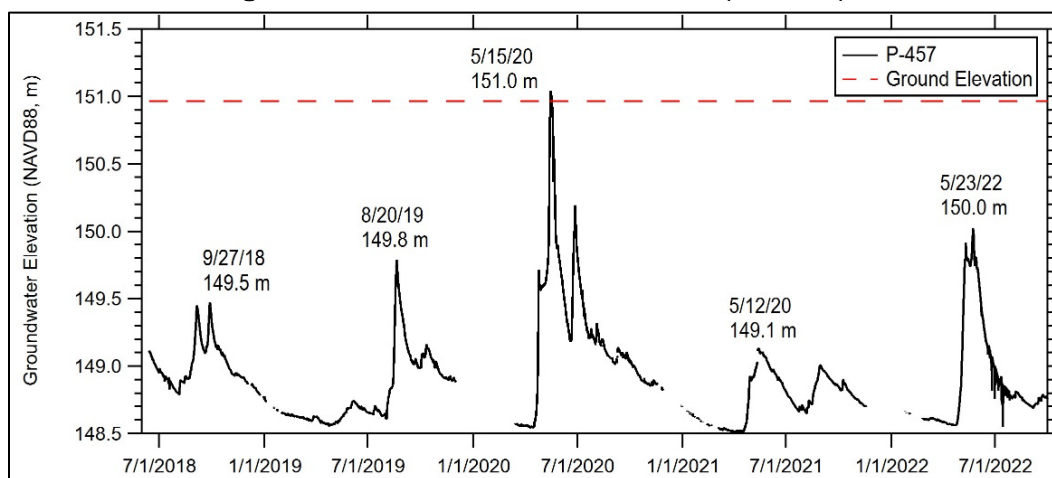
3.1.2 Relief well testing

During the relief well tests, a drawdown in water level elevation occurred (Figure 24). On 30 June and 1 July 2022, the relief wells closest to the piezometers with automatic sensors (306+50, and 308+00) were tested. The drawdown at the toe of the stability berm (P–457) during the 30 June testing of relief well 306+50 was 0.22 m. No changes in groundwater level at this piezometer was detected during the pumping at stations 290+25, 289+50, 291+00, 292+50, and 293+50. Therefore, it is estimated that groundwater elevation changes during the relief tests in this area are detected about 400 m distance from the piezometer cluster (P-351, P-457, and P-458). A contractor performed groundwater pumping at station 292+50 at the end of July which also impacted groundwater levels.

Figure 24. Groundwater elevations at P-457 (*black line*), relief well test dates (*light blue bars*; not all labeled, see Figure 7 for more information about station location and dates for each test), and precipitation (*gray bars*) at the MCD meteorological station.
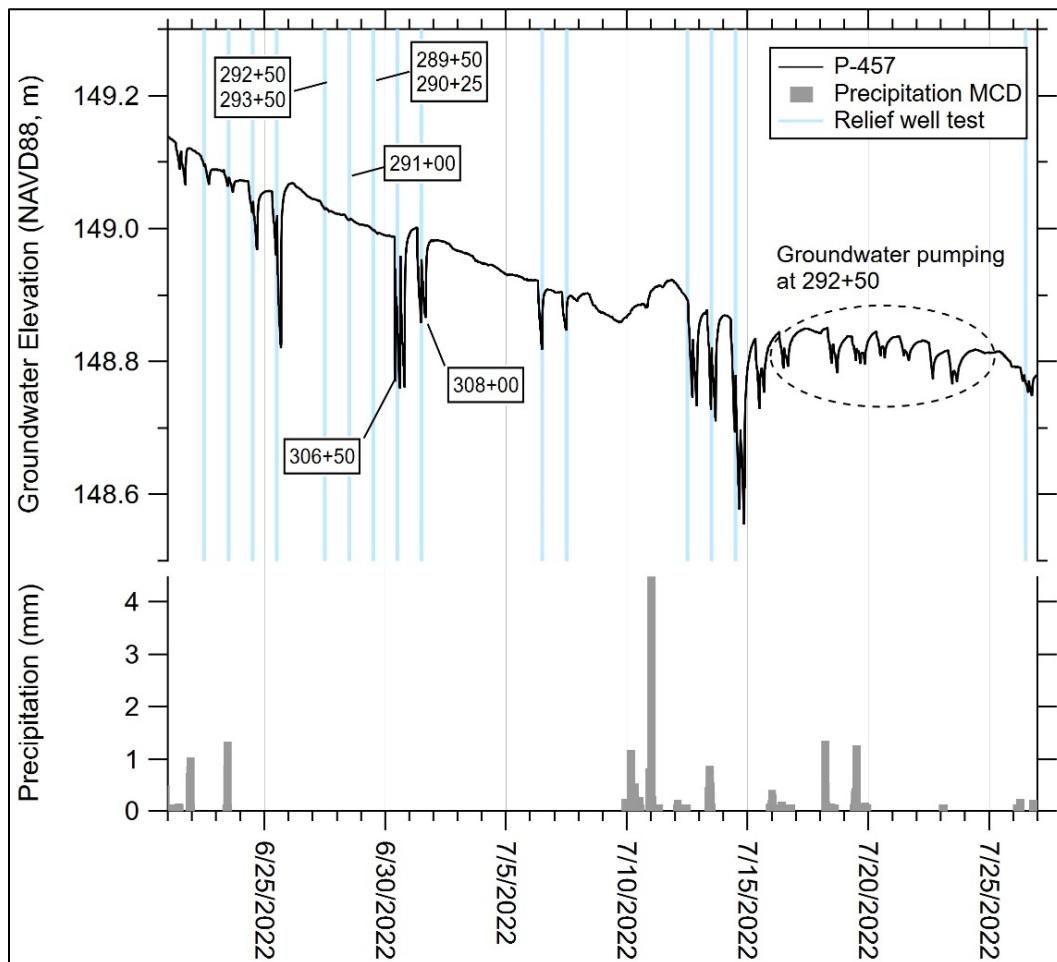
3.1.3 Soil temperature measurements

For the last few years, hourly soil temperatures have been measured at a nearby location (about 9 m west) to the fiber optic cable line (MW-100, Figure 3) with digital temperature sensors every 0.3 m from the ground surface down to about 15 m (Figure 25). When the relief well tests were performed in the vicinity of this location, changes in soil temperatures were evident. For example, when tests were performed at Stations 299+25 and 299+50 (July 7 and 6, respectively), the soil temperatures at a depth of 0.30 m increased about 6°C. It is also evident that precipitation, and an increase in groundwater levels, also influence the soil temperatures.

Figure 25. Soil temperatures (Monitoring Well [MW]-100; *blue, red, green, orange, turquoise, green, and pink lines*), groundwater elevation (P-457; *black line*), precipitation (MCD meteorological station; *gray bars*), and relief well test dates (*light blue bars*) between *(a)* 20 June and 1 October 2022 and *(b)* 30 June to 15 July 2022.
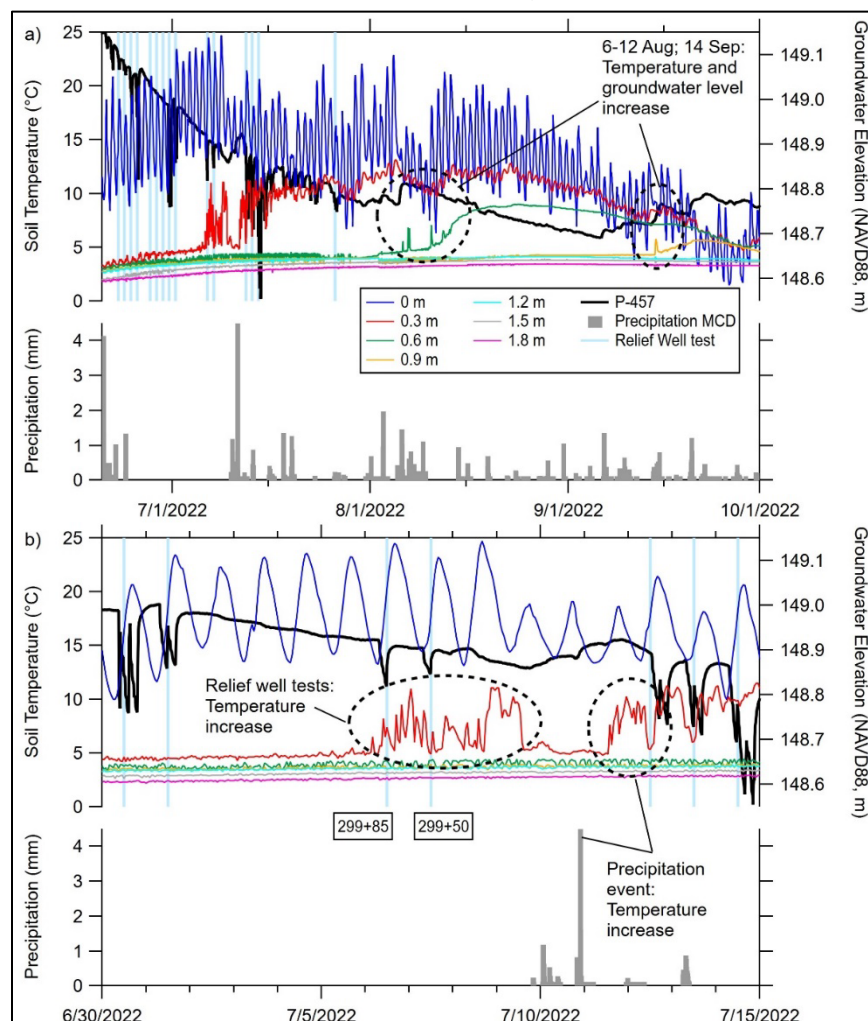
3.2 Fiber optic temperature monitoring

During the summer 2022 testing, we recorded subsurface temperature at every 25 cm totaling about 2,000 measurements per time step along the length of the fiber using the ruggedized DTS. Data was downloaded manually on site and subsequently sent to Silixa for joint analyses with HydroResearch. Following data quality assurance and quality control, temperature traces were uploaded to XSeepT™ for visualization and analyses.

The temperature measurements confirm that the cable installation was adequate, not showing any significant signal losses. The data indicates that the setup allows good monitoring accuracy. However, the applied monitoring frequency is higher than needed. Measuring each 2–4 hours is sufficient, and therefore recommended.

As expected, temperature data variation trends are similar along the length of the dam monitored (Figure 26). In general, temperatures varied about five degrees Celsius early summer, and at the end of fall (1 October), the temperatures varied less than 2 degrees (5°C to 6.8°C). An increase in soil and water temperature of up to 13°C was detected during the testing of the relief wells. This increase in temperature is along about 100 m fiber optic line (between Sta 306+50 and Sta 303+50) and it is in a location of known distress (Figure 3).

Figure 26. Temperature measurements along the fiber optic line for select dates (*blue, red, green,* and *black line*) *(a)* and from 30 June to 16 July *(b)*.
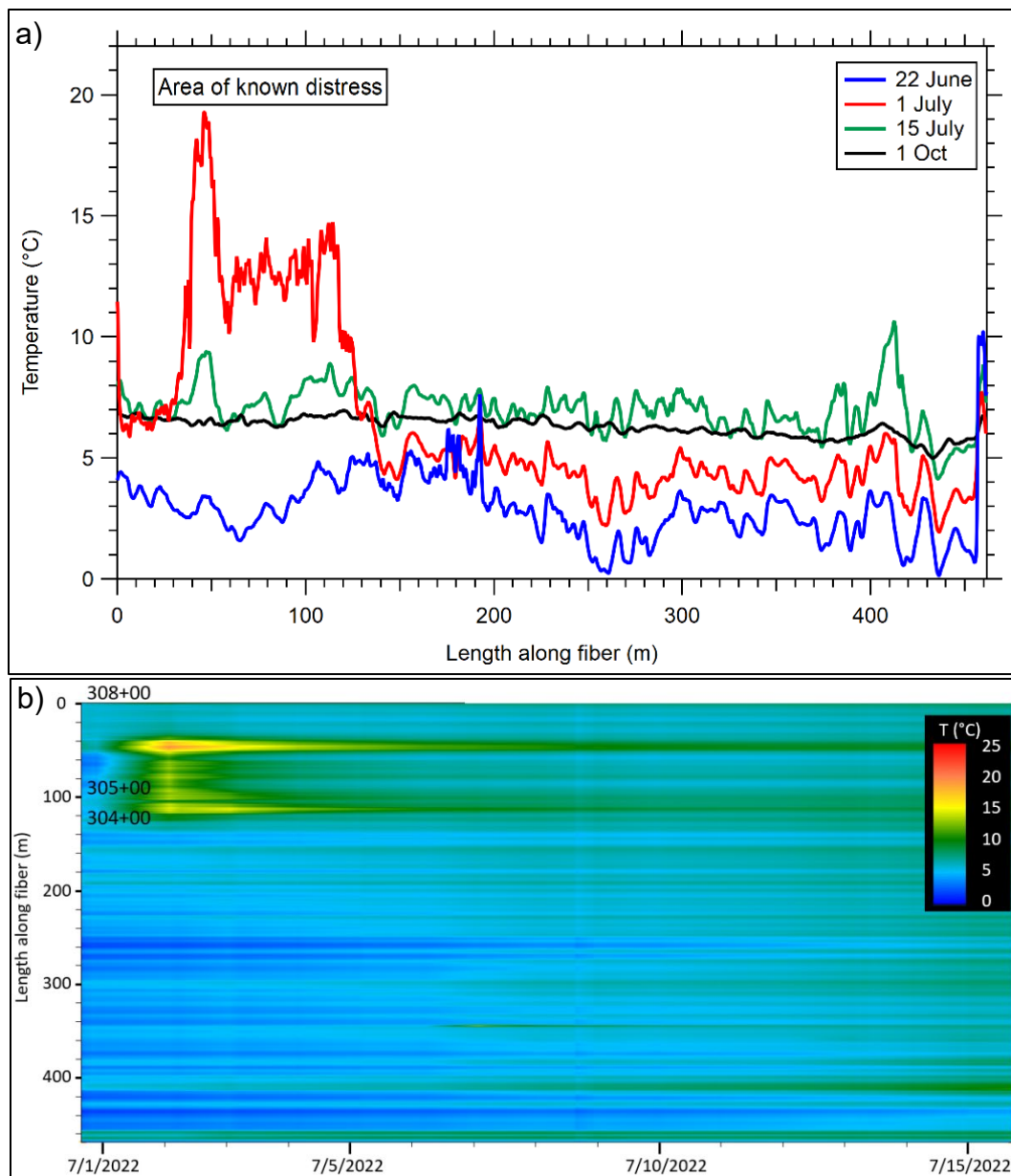
3.3 Simulation results

To calibrate the downstream water level of the model, we ran one simulation with no flood event (Section 3.3.1). The simulation results were compared to measured temperatures and pressure. To detect critical regions where a defect could appear, a high reservoir level was applied (Section 3.3.2). Finally, simulations of flooding were performed, describing the most realistic scenario (Sections 3.3.3 and 3.3.4). The 3D

simulations included a region of higher permeability (a defect), enabling the estimation of the seepage detection limits based on temperature.

3.3.1 No flooding

Assuming no flooding, the modeled temperature at the cable location as well as measured temperatures are shown in Figure 27 (Day 0 = January 1). The measured data is the average of the temperatures at Sta 305+00, 303+00, 302+30, 301+00, 300+00, 299+00, 295+00, 293+00, and 291+75. Both temperatures show a clear peak at the end of summer, even if there is a slight time shift between them. Uncertainties in parameters and boundary conditions contribute to this difference. However, the comparison indicates that the simulation captures the essential features of the heat transport in the dam.

As a part of the MCD monitoring network, water pressure measurements were collected at P-351, P-457, and P-458 (Figure 28). The hydraulic head computed from the pressure measurements during summer 2020 is shown in Figure 29*a*. The modeled pressure at similar positions is shown in Figure 29*b*.

Figure 27. Modeled cable temperature from last year (2022) and second to last year (2021, *solid blue* and *dashed green lines*, respectively, in excellent agreement). The air temperature input and DTS data from 2022 are also shown.
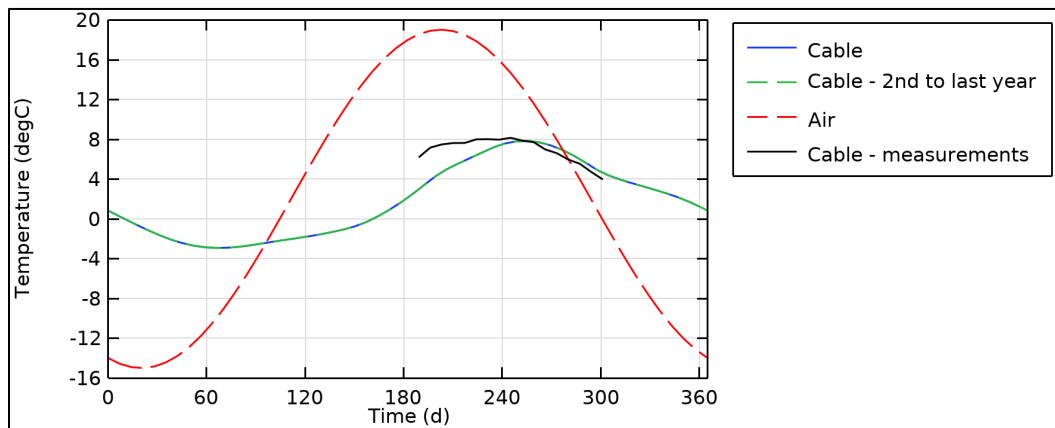
Figure 28. Locations of probes P-351, P-457, and P-458 on an aerial photo *(a)*.
They measure the pressure at elevations +146.3, +143.4, and +144.1 m,
respectively. The sketch illustrates the assumed locations of the fiber optic cable
in the model *(b)* (*red dots*).
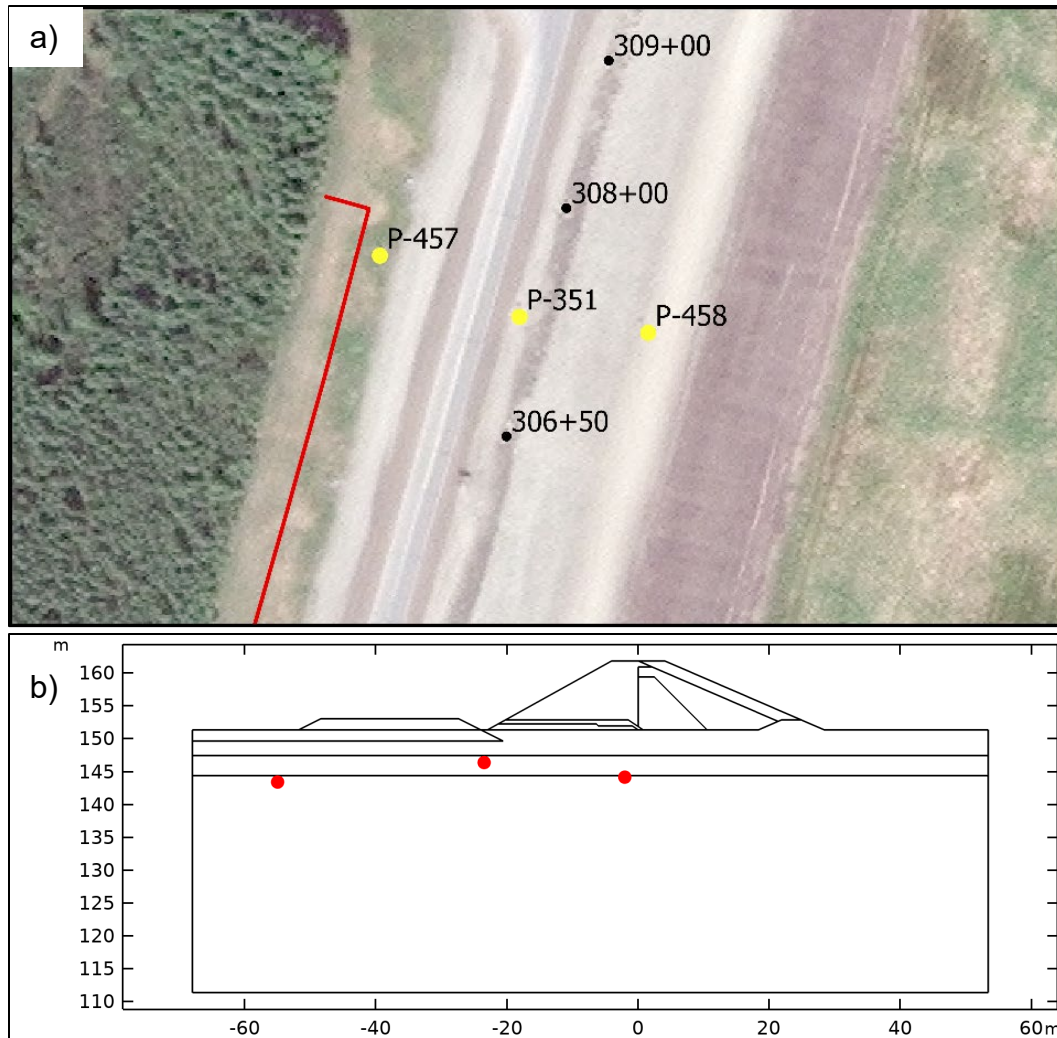
In general, P-351 has the highest pressure and P-457 the lowest. In the simulation, the most upstream sensor has the highest pressure and the most downstream the lowest (P-458 and P-457, respectively). The recorded data also have variations and higher values during the recorded period because of flooding. Since a constant water table elevation was imposed at the boundary of the model, a steady modeled pressure is expected.

The three probes show roughly the same values (within 0.1 m) in all three locations, both at flooding and no flooding (Figure 29a). The modeled pressure shows a similar pattern. Measured data at the beginning of November is assumed to be representative of the no flooding simulation

setup, which has a hydraulic head of about 149 m. This agrees well with measured pressures.

Figure 29. Hydraulic head, computed from piezometric measurements during 2020 *(a)* (cf. Figure 23) and modeled pressure at no flooding conditions *(b)*.
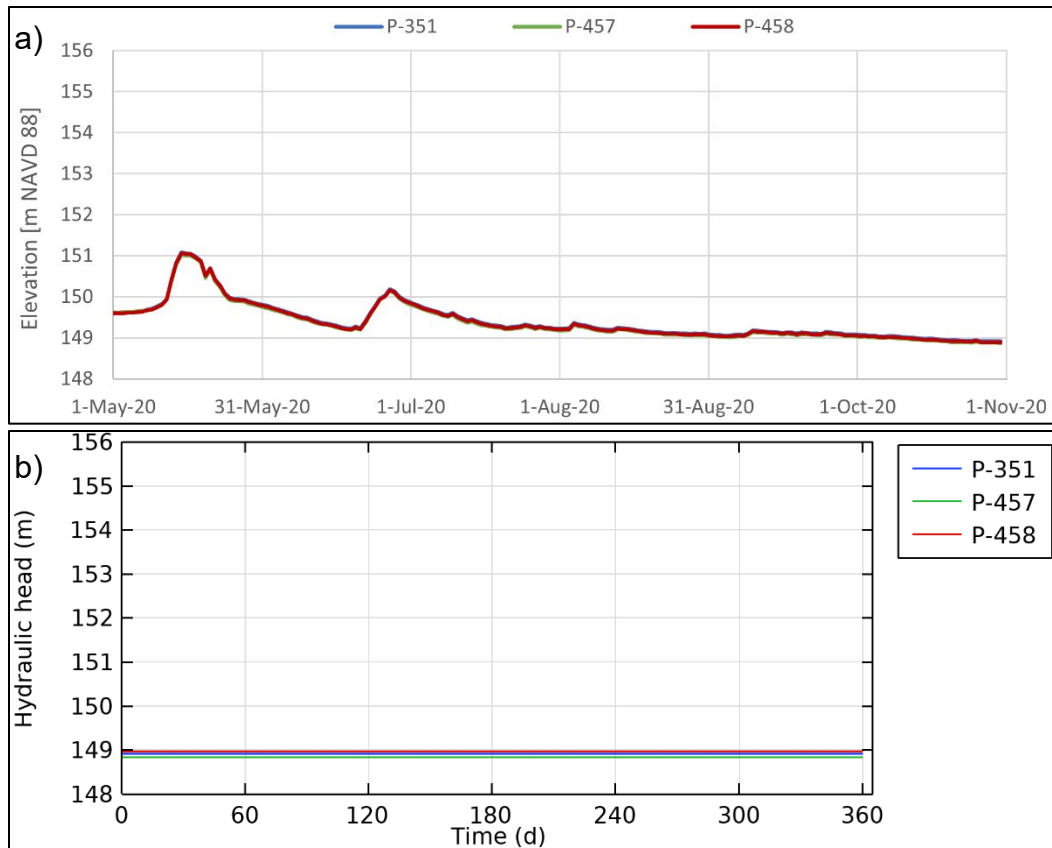
3.3.2 High reservoir level

The dam temperature at the end of December for a high reservoir level is shown in Figure 30. The figure also includes the water table, freezing level (shown as −0.1°C), and streamlines (*white*, *black*, and *gray* lines, respectively). At this date, the air temperature is close to its minimum, and the material at the material-air boundary is frozen. The dam surface in contact with the water is close to 0°C. In the dam, a region with temperatures greater than 0°C is reduced as the winter progresses. Below the top foundation gravel layer, the foundation does not freeze.

The water table elevation declines over the dam. However, it is still above ground level at the beginning of the stability berm, similarly as reported by USACE (2016).

Figure 30. Dam temperature on day 360 (27 December) in the simulation (on the fifth year). The water table, freezing level, and streamlines are also shown (*white, black,* and *gray lines*, respectively). The freezing level was assumed to be −0.1°C (i.e., slightly lower than the imposed reservoir temperature).
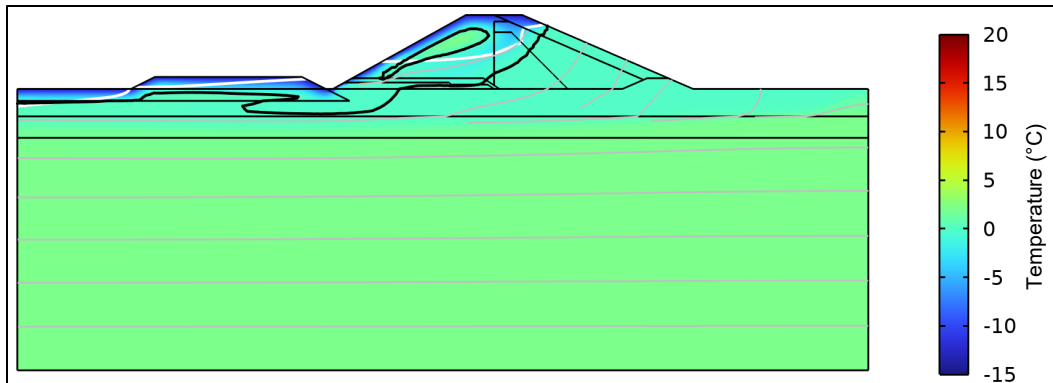
The modeled cable temperature is shown in Figure 31. Compared to when there is no flooding (Figure 27), the cable temperature is high. The ground is saturated close to the surface, which increases its heat conductivity. A large conductivity enables fast temperature changes of the region around the cable. Correspondingly, the temperature at the cable location is like that of the air. However, there is still approximately a 30 day shift between the air and cable temperature peak.

The region influenced directly by the water reservoir temperature is illustrated in Figure 32. Only temperatures between 0°C and 10°C are shown in the middle of August. Air temperatures are above this interval at this date. Therefore, temperatures in regions primarily affected by air temperatures are excluded. Below the top foundation gravel layer, the temperatures are low, indicating that the influence of the water reservoir there is limited.

Figure 31. Modeled cable temperature from the last year (2022) and second to last year (2021) at high reservoir level (*solid blue* and *dashed green lines*, respectively, in excellent agreement). The water and air temperature inputs are also shown.
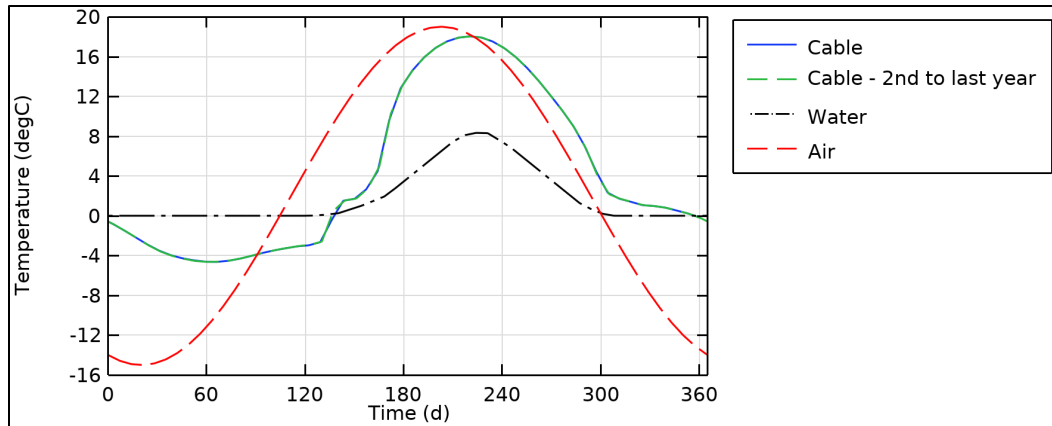
Figure 32. Dam temperature and streamlines (*gray lines*) at day 227 (16 August).
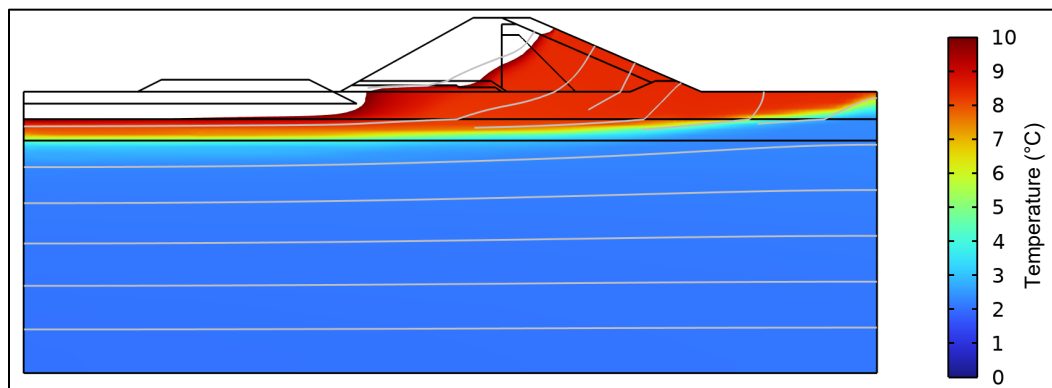
The most probable location for a defect to occur is in the region influenced by the water reservoir temperature. In this region, water flowing from the reservoir could cause internal erosion.

Modeled hydraulic heads at positions corresponding to P-351, P-457, and P-458 are presented in Figure 33. There is a larger difference between the heads than in Figure 29. Also, the water table at P-351 and P-457 is much higher than the recorded heads in Figure 29*b*. The larger spread indicates that the flow behavior at the high water level is significantly different. The hydraulic heads are almost constant but change slightly due to the temperature dependency of the dynamic water viscosity.

A grid refinement study was also performed with the high reservoir level. Except from the regular mesh described in Section 2.4.1, the simulation was also run with grids using a finer (more elements) and a coarser (fewer elements) mesh, in comparison to the regular grid. The

fine and coarse grids had half and twice the maximum element size, respectively. The maximum allowed time step was 2 h for the simulation with the fine grid. The cable temperatures during the last year are shown in Figure 34 for the three grids. Some differences can be seen, especially around day 160 (10 June). However, the overall time dependency is similar for all three grids. Also, the lowest and highest temperatures and the phase shift of the temperature peak agree well. Therefore, the comparison indicates that the conclusions from the simulation results are almost independent of the grid selected.

Figure 33. Modeled hydraulic head at positions corresponding to P-351, P-457, and P-458.
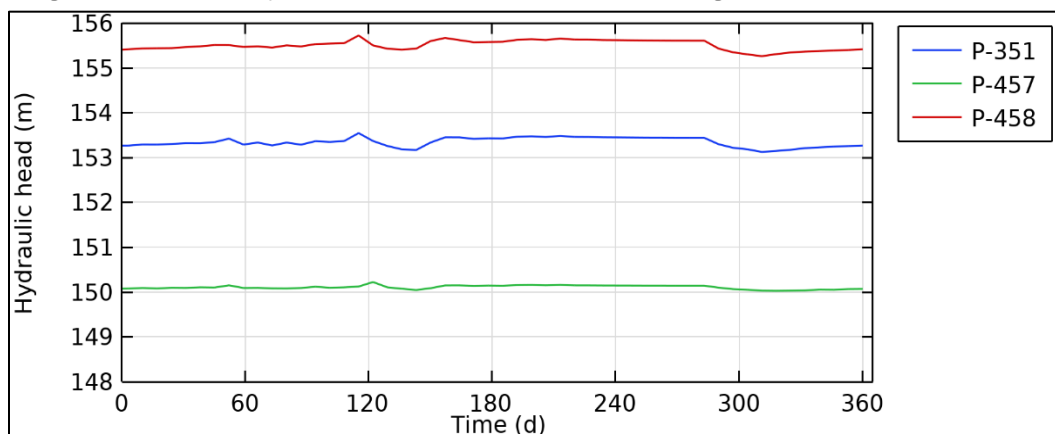
Figure 34. Cable temperatures at high reservoir level for three different grids.
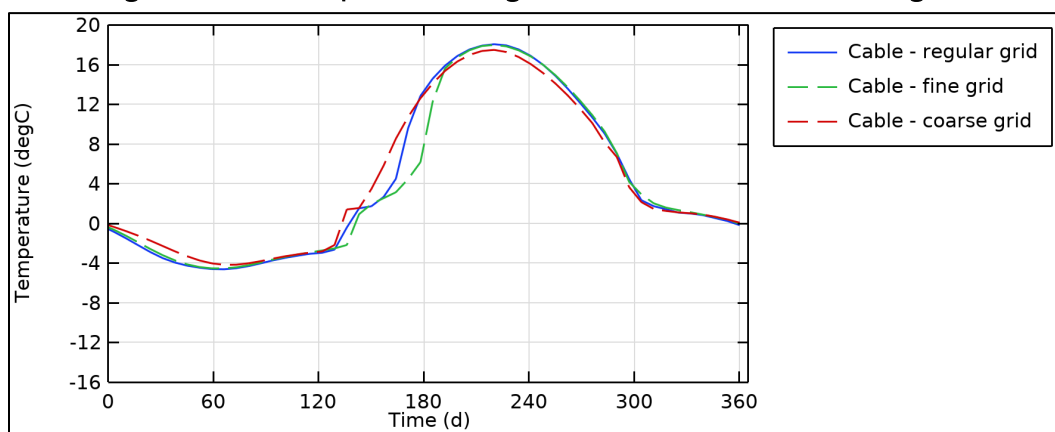
3.3.3 Flooding of 2D model

The modeled cable temperature is shown in Figure 35 for a year with flooding. The maximum cable temperature and its phase shift are in between those found for the constant high reservoir and no-flooding simulations. The hydraulic heads at positions corresponding to P-351, P-

457, and P-458 are presented in Figure 36. They show a clear peak corresponding to flooding. The imposed upstream water table level is also shown in the figure (same as in Figure 21).

In this simulation, the upstream water pressure was applied with the pervious layer boundary condition. To check that the water pressure was correctly imposed, the measured pressure was compared with the theoretical distribution (Figure 37). There is a satisfactory agreement between the applied and measured pressure from the bottom of the model to the water table (water pressures above 0 Pa).

The flow velocity magnitude for day 178 (28 June, rising water level) is shown in Figure 38. The velocity above the water table (unsaturated zone) is close to 0 μm/s. The foundation gravel layers, and the drain have a large velocity due to their high permeability.

Figure 35. Modeled cable temperature from last year (2022) and second to last year (2021) at flooding (*solid blue* and *dashed green lines*, respectively, in excellent agreement). The water (*dashed dotted black line*) and air temperature *(dashed red line)* inputs are also shown.
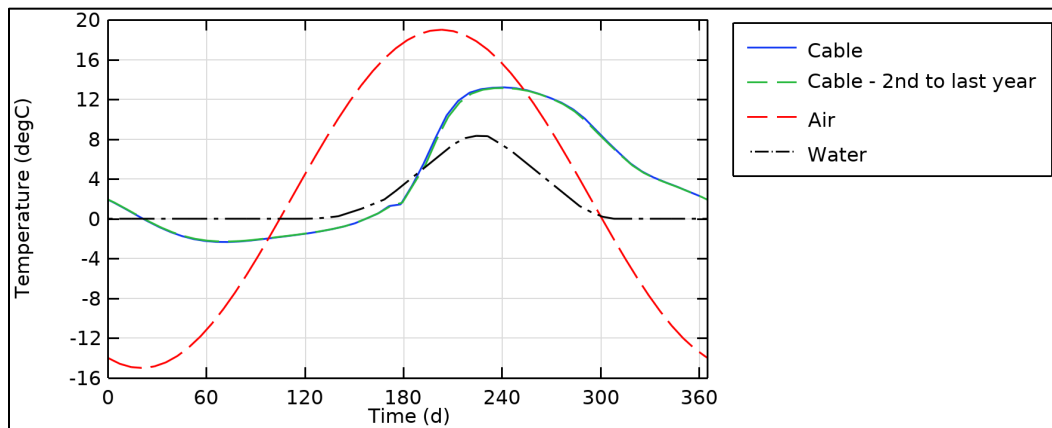
Figure 36. Modeled hydraulic head at positions corresponding to P-351, P-457, and P-458. The upstream water table level is also shown (*black dotted dashed line*).
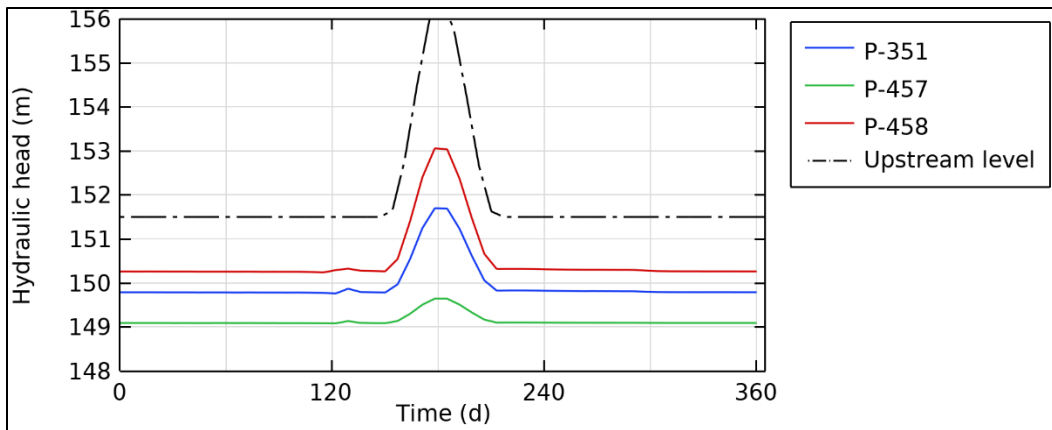
Figure 37. Water pressure on the boundary where the pervious layer boundary condition is applied, shown at five different times (with 14-day difference) during which the upstream water table elevation changed. Imposed water pressure distributions are shown with *black dotted lines*, valid above 0 Pa.
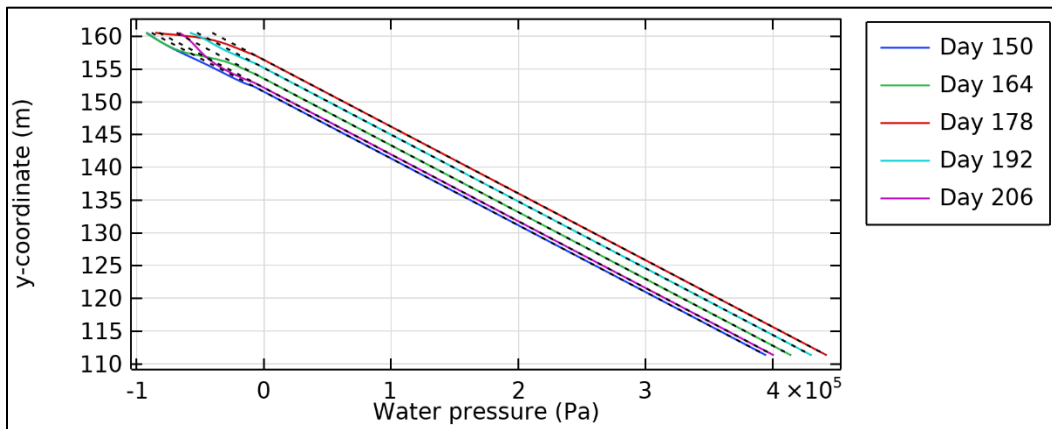
Figure 38. Velocity magnitude (μm/s) at day 178 (28 June). The color bar is limited to show 0 μm/s–50 μm/s. The water table is indicated with a *white line* and streamlines with *gray lines*.
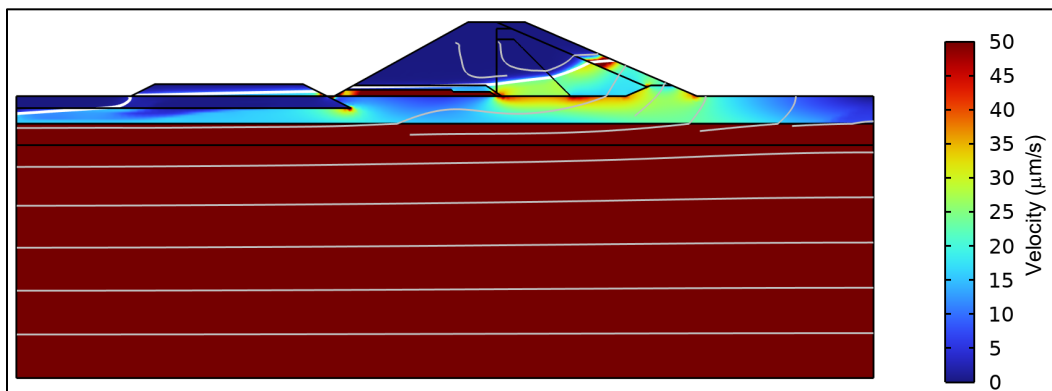
3.3.4 Flooding of 3D model with a highly permeable region

For the 3D simulations, the time-dependent effects of velocity and pressure fields were omitted (see Section 2.4.2). The Richards' equation was instead solved several times with stationary boundary conditions, specifying different upstream water table levels. To simulate a quickly rising reservoir, heat transfer at flooding was described by using a steady velocity field at a low water table level and then, at day 150 (31 May 2022), switching to a high-water level velocity field.

A highly permeable region (a defect, see material properties in Section 2.4.2), in the form of a cylinder-shaped channel, was introduced to simulate a critical region. Its center was placed at $z = 0$, making use of the symmetry condition (Section 2.4.3). The velocity magnitude for low and high-water levels are shown in Figure 39. The highly permeable region is clearly visible (i.e., higher velocities) at the high-water level.

The temperature measured at the location of the cable at the high-water level is shown in Figure 40. There is around a 1°C temperature difference between the defect region and the other side of the model ($z = 0$ and 15 m, respectively).

To demonstrate the spatial difference in temperature, we show the temperatures at $z = 0$ and 15 m at the cable, as well as 4 m below the fiber optic cable and at the dam toe (Figure 41). There is a difference in the highest temperature at the cable of approximately 2 °C induced by the defect (around day 230). The location 4 m below the cable is close to the center of the defect (in the y-direction). The phase shift between the temperature at $z = 0$ and 15 m is more pronounced there (Figure 41b). The dam toe is closer to the defect inflow point. However, the temperature's x-dependency seems to be weaker than the y-dependency. It is possible that this effect is a result of the large flow velocity at the defect, and therefore it leads to fast heat transport in the streamwise direction.

Figure 39. Velocity magnitude (µm/s) for low *(a)* and high water level *(b)*. The color bar is limited to show 0 µm/s–500 µm/s. The water table is indicated with a *white line*.
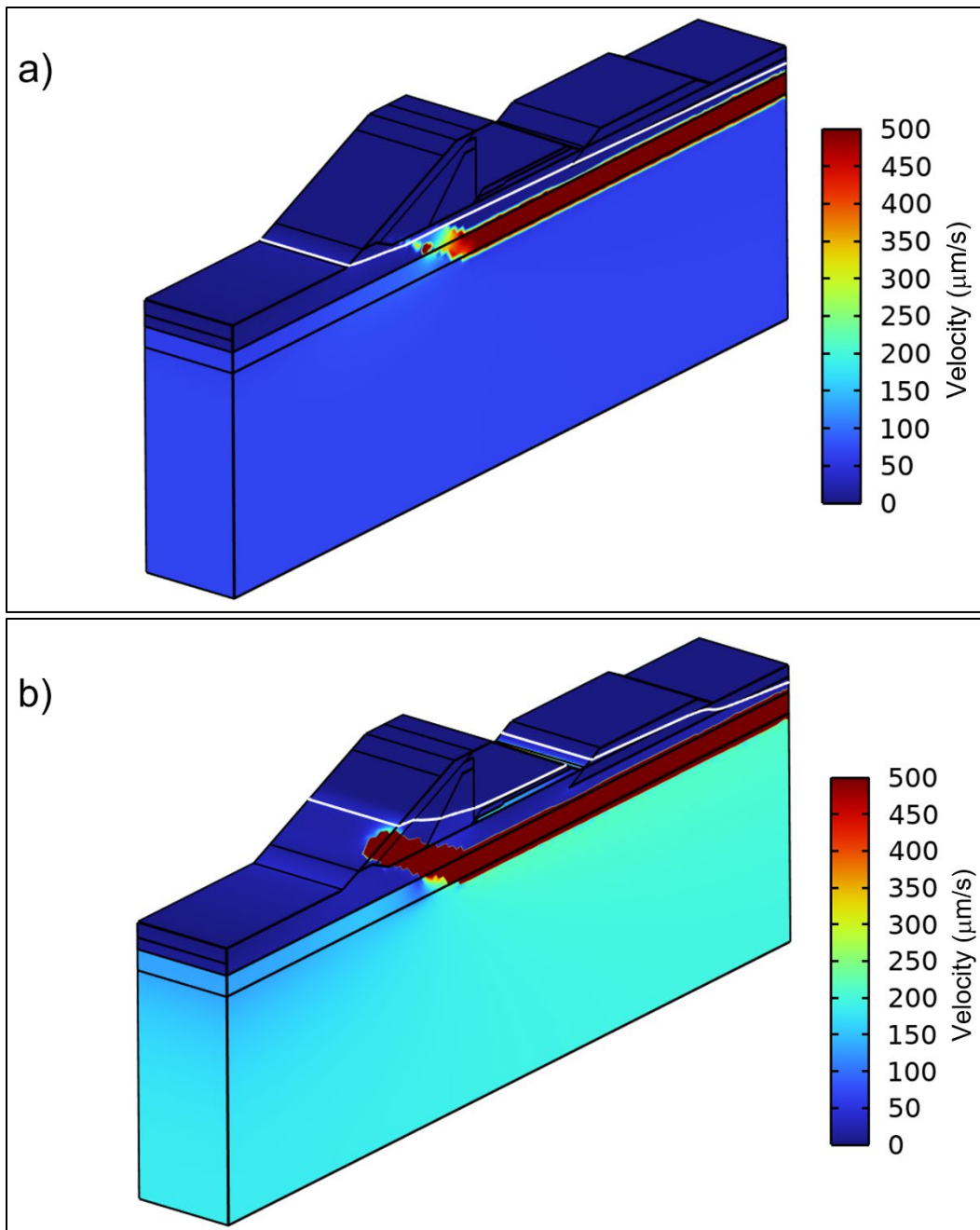
Figure 40. Measured temperature at the high-water level at different dates.
(Day 150 = 31 May; Day 185 = 5 July; Day 220 = 9 August; Day 255 = 13 September;
Day 290 = 18 October; Day 325 = 22 November; Day 360 = 27 December.)
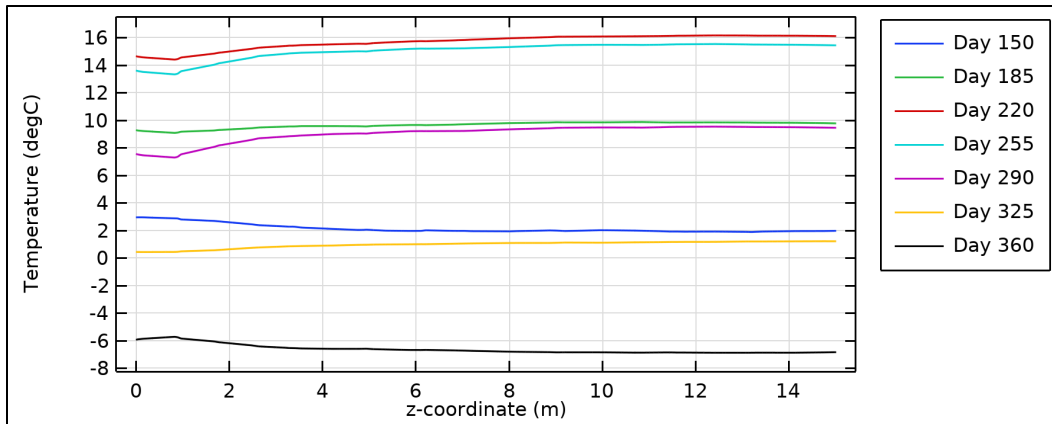
Figure 41. Spatial location of temperature measurements *(a)* (*red dots*). These locations include the position of the cable, a line 4 m below the cable, and a location below the dam toe. Temperature for several locations *(b)* as shown with *red dots* in (*a*).
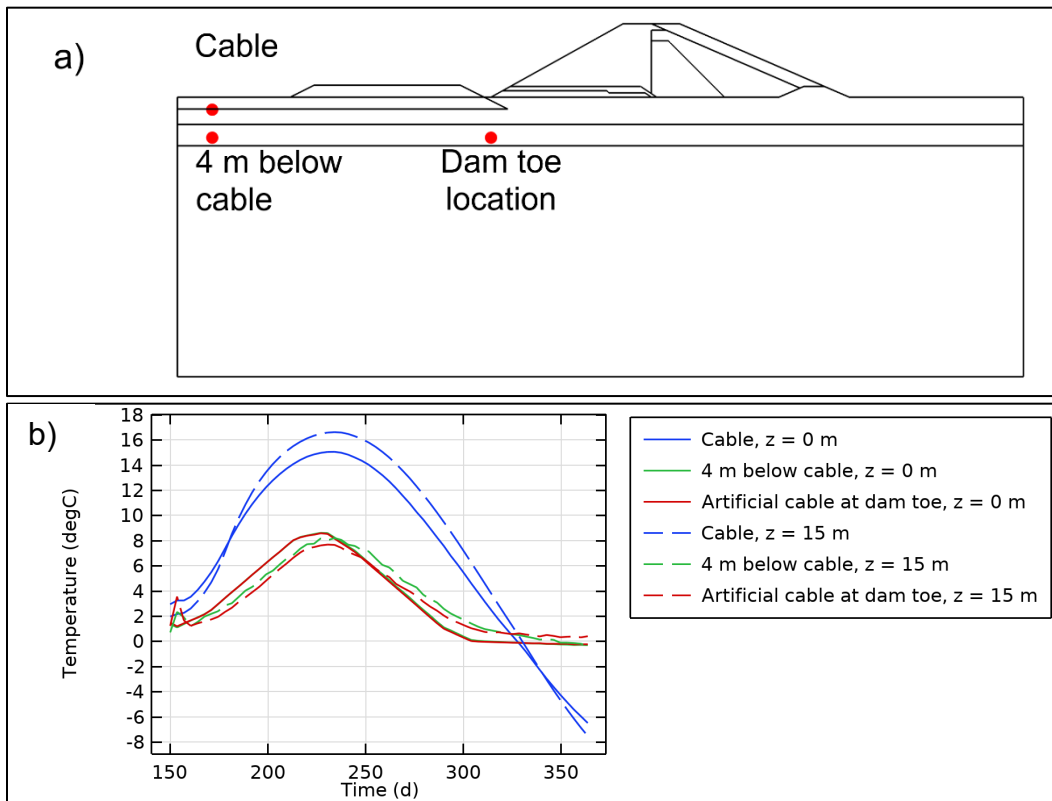
A temperature waterfall plot is shown in Figure 42, constructed from the temperature at the cable location. The highly permeable region is apparent around $z = 0$ m by the reduction in temperature it induces. The mean

temperature (*red trace*) at the higher permeable region is lower compared to the other non-disturbed regions.

Figure 42. Temperature map from the location of the cable installation at a high-water level.
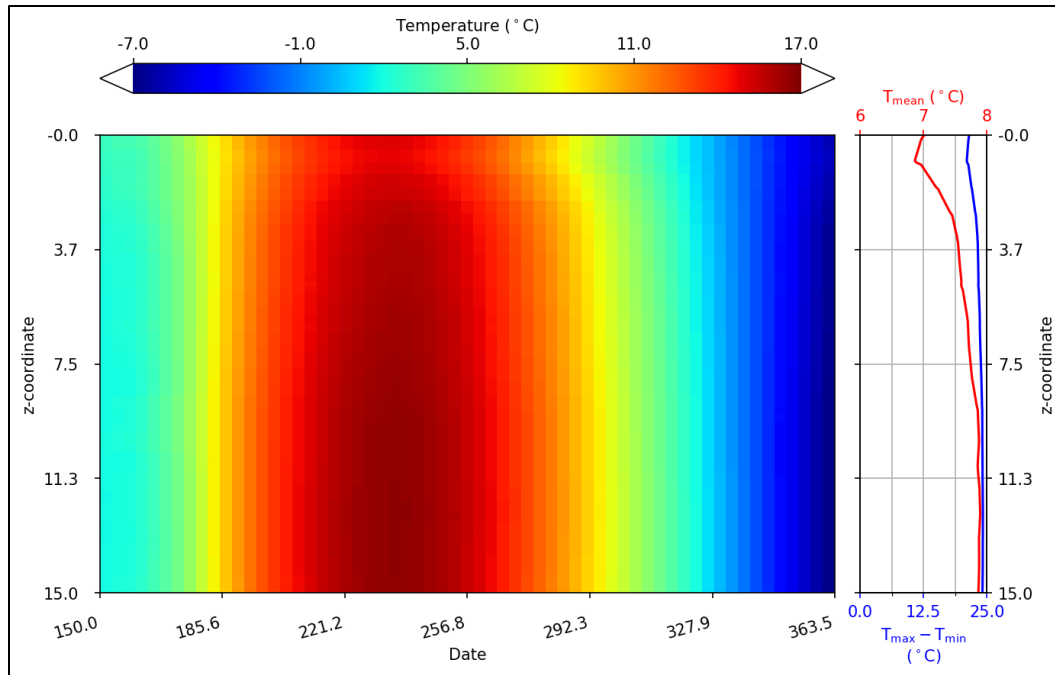
3.3.5 Seepage flow rates and temperature response

The thermal response at different seepage flow rates in the concentrated seepage zone is trivial when heat conduction from the surface can be ignored. If surface heat conduction is unimportant, the natural seasonal water temperature variation offers excellent conditions for seepage evaluation, especially at constant water levels (i.e., constant seepage flow rates during the year). At the current site, we have flooding events with short-term water level changes, water temperature variations, and significant heat conduction. All these factors have been simulated, and therefore we can present a relation between seepage flow and measured temperature.

Significant seepage also occurs in deeper layers. The risk of internal erosion there is believed to be low, but it is important to note that the seepage flow in the deeper layers also impacts the temperature in the layers above.

We computed the downstream flow rate Q, excluding the bottom gravel layer (Figure 18). The flow at the highly permeable region was estimated

as the difference between Q and the corresponding flow $Q_0 = 9.6 \cdot \times 10^{-3}$ m³/s without a highly permeable region ($\Delta Q = Q - Q_0$). It should be noted that ΔQ only is half the flow of a circular permeable region. The maximum temperature difference ΔT_{max} between $z = 15$ and 0 m at the location of the fiber optic cable was used to quantify the defect's temperature effect (cf. Figure 41). The simulations were also repeated with the permeability changed by a factor of 1/2, 2, 4, and 8. The flow increases with the permeability (Figure 43) where the maximum temperature difference exceeds 2.0°C for flow rates above $\Delta Q = 0.01$ m³/s. As the defect radius is 2 m and the model 15 m in the z-direction, the corresponding relative flow-rate change can be estimated to $(\Delta Q/2$ m$)/(Q_0/15$ m$) = 7.8$. Temperature anomalies above 2.0°C are identifiable, indicating that seepage flow rates increased with a factor 7.8 (or above) from the base flow rate could be detected.

Figure 43. Maximum temperature difference between $z = 0$ and 15 m at the location of the fiber optic cable, ΔT_{max}, and flow due to a higher permeable region, ΔQ.
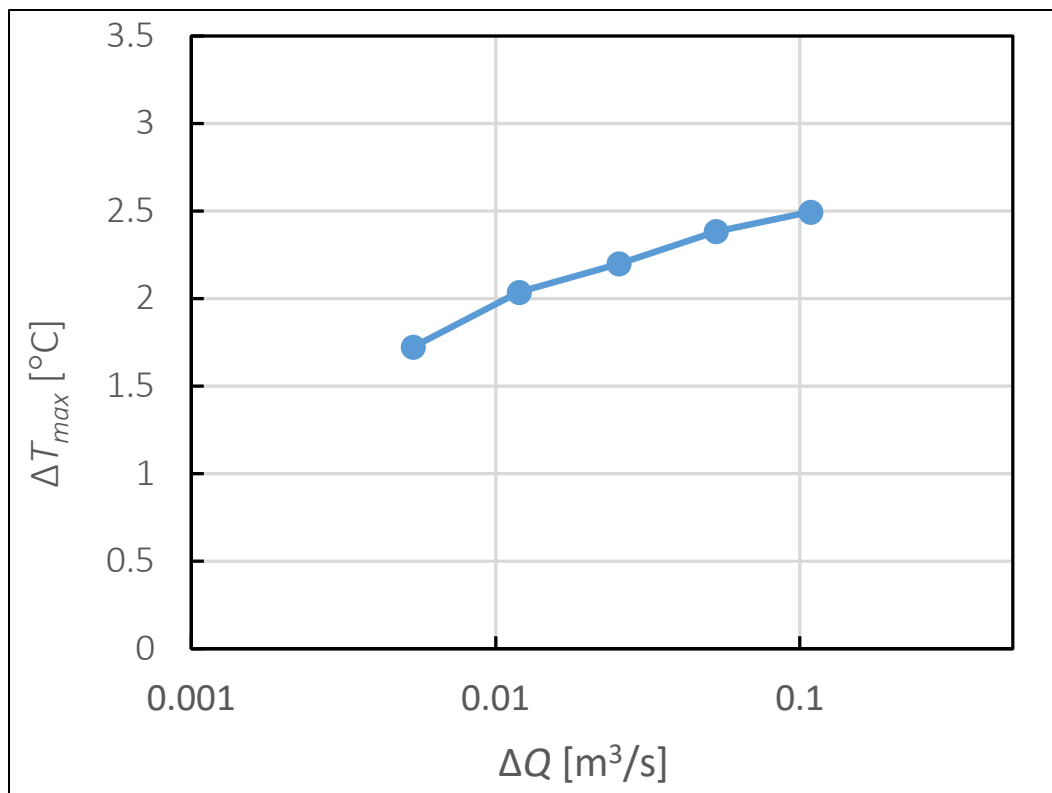
3.4   Estimated installation and initial monitoring cost at MCD

The cost of installation is greatly dependent on the location, site conditions, and length of installation. We performed a simplified cost analysis of installation and initial setup of a monitoring system. Our estimated cost of installation is $270 per meter. This cost estimate is for a total length of about 6,400 m along the MCD. It includes the fiber optic cable, trenching and installation of the fiber optic cable, and two DTS systems. An initial setup of the monitoring system and linking the DTS data to the existing network is also encompassed in this cost. The total cost listed excludes any electric utility service connection and running the fiber cable into the control works. It is important to note that Fairbanks, Alaska, is in the Interior Alaska, which is in a remote location when considering the availability of trenching equipment. Additionally, Fairbanks is in discontinuous permafrost which can also result in higher cost.

4 Conclusions and Recommendations

Visual inspections are performed at dams to aid detecting possible seepage or other evidence of water migration at dams. Furthermore, monitoring wells that measure soil and water properties in localized areas are commonly deployed to monitor subsurface conditions. However, because monitoring wells are only a reliable means of monitoring local subsurface soil and water conditions, and there is a time constraint to visual inspections, fiber optic distributed sensing-based systems are better suited to this task. DTS can continuously monitor kilometers of ground and therefore improving the odds of seepage detection over both visual inspection and monitoring wells.

The principal advantages of distributed temperature measurement are automated high spatial (i.e., meters) and temporal (i.e., hours) resolution over large distances, up to 10 km. Integration of fiber optic cable into an existing dam embankment can be done relatively easily within or near the toe of the dam. For dam reinforcement projects, where a downstream toe-berm is constructed, inclusion of a fiber optic cable in the design can provide a means to monitor the effectiveness of the repair. The seepage monitoring would ideally be carried out in the inflow and outflow filters making this the optimal placement of the fiber optic cable during new constructions.

There are many additional advantages of fiber optic temperature sensing techniques. Some of these advantages are (Vogel et al. 2001)

- easy installation,
- large spatial coverage,
- no active electronic circuits along the cable,
- long-term monitoring,
- repeatability at any time interval,
- can be used in corrosive environments, and
- low-cost installation hardware (cable).

In addition, the same cable used for temperature-based seepage monitoring can also be simultaneously used for distributed strain sensing for monitoring structural movement and distributed acoustic sensing for time-lapse active or passive seismic monitoring by incorporating multiple optical fibers.

4.1   Conclusions

In the summer of 2022, a fiber optic monitoring test section was installed in a known area of distress at MCD. The purpose of this installation was to test the ability of fiber optics to detect the movement of water from the upstream to downstream side of MCD by measured changes in groundwater temperature. Dam failures are often preceded by signs of water migration, which can include water level and temperature properties.

No flood events occurred during the 2022 monitoring season. Therefore, evaluation of the time-series data at selected locations indicates similar thermal behavior along the fiber optic line. Some larger deviations in temperatures were attributed to other dam safety monitoring events which included relief well testing in the vicinity of the test site. In fact, an increase in soil and water temperature of about 13°C was captured in the continuous DTS temperature measurements. This increase in temperature was detected in an area (about 100 m along the fiber optic line) of known distress that occurred from flood events in 2014. Temperate response during hydraulic testing in nearby relief wells positively confirmed the ability to capture advective temperature signal in areas where changes would not have been detected by current monitoring methods.

To achieve optimal fiber optic cable placement, and to understand temperature sensitivity to seepage in complex thermo-hydraulic environments, numerical modeling can be carried out prior to installation or post-installation to aid with data analyses. Modeling helps to understand the thermal response in groundwater and seepage paths within and downstream of the dam. The results of this modeling can be used to identify optimal location and depths for cable installation. With a 2D model, where both flooding and no flooding scenarios were simulated, good agreement was achieved between measured and simulated temperatures. 3D simulations showed how a defect affected the temperature at rapid flooding. The defect represents lost fines by internal erosion or local and natural heterogeneities.

The 3D modeling indicates that significant temperature deviations would be present at the existing cable location for seepage flow rates about eight times higher than the base flow. The rapid flooding was assumed to occur at the end of May. At a later flooding date, the seepage water would be warmer, but also the temperature at the cable region would be higher

because of heat conduction. Therefore, the detectable seepage level could depend somewhat on the flooding date. This dependency could be investigated with additional simulations.

Temperature monitoring at dams built for flood protection in the United States has so far not been applied as we are aware. The short time duration of the flood, which may occur at different times of the year, limits the temperature change due to seepage flow. However, due to the high seepage flow rate in this case, we will still see a significant temperature signal at local higher flow. This information will be achieved at high resolution along the entire dam.

4.2 Recommendations

Based on the technology review and case study at the MCD, it is recommended that dam installations consider using fiber optic DTS monitoring systems for early detection of seepage or to monitor changes in seepage on dams with known issues. Supplementing the current practice of visual dam inspection with distributed sensing-based monitoring may allow earlier detection of seepage deficiencies, thereby enabling the installation to intervene early, reduce risk and better manage infrastructure investment. Further, by installing multi-channel fiber optic cable for negligible cost increases, monitoring systems can be augmented for distributed strain and acoustic monitoring in seismically active areas.

The length calibration of the optical cable used here is based on drawings and some coordinates. Additional cable coordinate (and Sta) measurements could improve the calibration. The best way is normally to measure the coordinates (and create Sta values) with intervals of 10 m, following the markings on the cable. This method is difficult to apply at plow installations, but possible with some modifications. Therefore, we recommend this at future installations. The temperature measurements confirm that the cable installation was adequate, not showing any significant signal losses. The data indicates that the setup allows good monitoring accuracy. However, the applied monitoring frequency is higher than needed. Measuring each 2 hours to 4 hours is sufficient, and therefore recommended to partly save on energy requirements.

Cables should be placed where potential changes in seepage that may affect the safety of the dam are most likely to occur. Ideal locations will vary based on geological conditions, embankment geometry and construction materials, meteorological conditions, as well as typical pool elevations. Fiber optic installations are frequently applied in dams and dikes with water levels on the upstream side. Ideally, cables are installed at construction close to the dam core or deep below an added toe berm. The temperature variation will then be dominated by the seepage flow rate, allowing a high sensitivity in the order of 1 μm/s–10 μm/s. This will not be possible to achieve in this case. The selected cable location (and probably the only possible one at MCD) is further from the inflow area than usually desired. The seepage-induced temperature effects normally decrease with length and the impact from surface heat conduction becomes more pronounced. However, at the current installation, with considerable seepage flow, the temperature decrease will be smaller, and the location of the cable will then be less critical.

Modeling enables an improved understanding of the sensitivity of the method to detecting changes in seepage rate at MCD and similar flood control structures where saturation and seepage flow rates are highly variable throughout the year and from year to year.

Bibliography

Bolève, A., A. Revil, F. Janod, J. L. Mattiuzzo, and A. Jardani. 2007. "A New Formulation to Compute Self-Potential Signals Associated with Ground Water Flow." *Hydrology and Earth System Sciences Discussions* 4 (3): 1429–1463. http://dx.doi.org/10.5194/hessd-4-1429-2007.

Bridle, R. 2017. "Internal Erosion Mechanics and Risk Estimation Based on ICOLD Bulletin 164." In *Geo-Risk 2017: Geotechnical Risk Assessment and Management*, 137–146. https://doi.org/10.1061/9780784480724.013.

Dakin, J. P., D. J. Pratt, G. W. Bibby, and J. N. Ross. 1985. "Distributed Optical Fibre Raman Temperature Sensor Using a Semiconductor Light Source and Detector." *Electronics Letters* 21 (13): 569–570. https://doi.org/10.1049/el:19850402.

Gelvin, A. B, C. R. Williams, and S. P. Saari. 2019. *Web-Based Monitoring of Piezometers for the US Army Corps of Engineers Moose Creek Dam, North Pole, Alaska.* ERDC/CRREL TR-19-26. Hanover, NH: ERDC–CRREL. http://dx.doi.org/10.21079/11681/35293.

Johansson, S. 1997. "Seepage Monitoring in Embankment Dams." PhD Diss., Royal Institute of Technology. http://www.diva-portal.org/smash/get/diva2:8066/FULLTEXT01.pdf.

Johansson, S. 2011. "Numerical Modeling of Seepage and Temperature for Internal Erosion Detection in Embankment Dams." XI ICOLD benchmark workshop on numerical analysis of dams, Valencia, October 20–21, 2011.

Johansson, S. 2017. "Fibre-Optic Temperature Monitoring for Seepage Detection in Embankment and Tailing Dams." 85th Annual Meeting of International Commission on Large Dams, Prague, Czech Republic, July 3–7, 2017.

Johansson, S., and P. Sjödahl. 2004. "Downstream Seepage Detection Using Temperature Measurements and Visual Inspection—Monitoring Experiences from Røsvatn Field Test Dam and Large Embankment Dams in Sweden." Proc. Intl. Seminar on Stability and Breaching of Embankment Dams.

Kappelmeyer, O. 1957. "The Use of Near Surface Temperature Measurements for Discovering Anomalies Due to Causes at Depths." *Geophysical Prospecting* 5 (3): 239–258. https://doi.org/10.1111/j.1365-2478.1957.tb01431.x.

Kurashima, T., T. Horiguchi, and M. Tateda. 1990. "Distributed-Temperature Sensing Using Stimulated Brillouin Scattering in Optical Silica Fibers." *Optics Letters* 15 (18): 1038–1040. https://doi.org/10.1364/OL.15.001038.

Quinn, M. C. L., C. Engel, T. Coleman, S. Johansson, and C. D. P. Baxter. 2019. "Fiber Optic Temperature Sensors In Under-Documented Dams." In *Sustainable and Safe Dams Around the World*, 1184–1192. London: CRC Press. http://dx.doi.org/10.1201/9780429319778-102.

Sjödahl, P., T. Dahlin, and S. Johansson. 2009. "Embankment Dam Seepage Evaluation from Resistivity Monitoring Data." *Near Surface Geophysics* 7 (5-6): 463–474. https://doi.org/10.3997/1873-0604.2009023.

Tyler, S. W., J. S. Selker, M. B. Hausner, C. E. Hatch, T. Torgersen, C. E. Thodal, and S. G. Schladow. 2009. "Environmental Temperature Sensing Using Raman Spectra DTS Fiber-Optic Methods." *Water Resources Research* 45 (4): 1–11. https://doi.org/10.1029/2008WR007052.

USACE (US Army Corps of Engineers). 2016. *Moose Creek Dam Preliminary Groundwater Hydraulic Modeling. North Pole, Alaska, Alaska District, Pacific Ocean Division. QCC Draft, PN: AK00085.*

USACE (US Army Corps of Engineers). 2018. *Geotechnical Monitoring and Instrumentation Plan. Moose Creek Dam, East Cutoff Dike and Tanana River Levee.* Chena River Lakes Flood Project, North Pole, Alaska, Alaska District, Pacific Ocean Division.

Vogel, B., C. Cassens, A. Graupner, and A. Trostel. 2001. "Leakage Detection Systems by Using Distributed Fiber Optical Temperature Measurement." *Smart Structures and Materials 2001: Sensory Phenomena and Measurement Instrumentation for Smart Structures and Materials.* https://doi.org/10.1117/12.435546.

Abbreviations

CS	Campbell Scientific
DTS	Distributed temperature sensing
ICOLD	International Commission on Large Dams
MCD	Moose Creek Dam
MM	Multimode
MW	Monitoring Well
P	Piezometer
SM	Single mode
SNOTEL	Snowpack Telemetry
Sta	Station
USACE	US Army Corps of Engineers

REPORT DOCUMENTATION PAGE

1. REPORT DATE October 2023	2. REPORT TYPE Final	3. DATES COVERED	
		START DATE FY21	END DATE FY22

4. TITLE AND SUBTITLE
Initial Data Collection from a Fiber-Optic-Based Dam Seepage Monitoring and Detection System

5a. CONTRACT NUMBER	5b. GRANT NUMBER	5c. PROGRAM ELEMENT
5d. PROJECT NUMBER	**5e. TASK NUMBER**	**5f. WORK UNIT NUMBER**

6. AUTHOR(S)
Anna M. Wagner, Arthur B. Gelvin, Jon B. Maakestad, Thomas Coleman, Dan Forsland, Sam Johansson, Johan Sundin, and Chandler S. Engel

7. PERFORMING ORGANIZATION NAME(S) AND ADDRESS(ES) US Army Engineer Research and Development Center (ERDC) Cold Regions Research and Engineering Laboratory (CRREL) 4070 9th Street Fort Wainwright, AK 99703	8. PERFORMING ORGANIZATION REPORT NUMBER ERDC/CRREL TR-23-15

9. SPONSORING/MONITORING AGENCY NAME(S) AND ADDRESS(ES) Headquarters, US Army Corps of Engineers Washington, DC 20314-1000	10. SPONSOR/MONITOR'S ACRONYM(S)	11. SPONSOR/MONITOR'S REPORT NUMBER(S)

12. DISTRIBUTION/AVAILABILITY STATEMENT
Distribution Statement A. Approved for public release: distribution is unlimited.

13. SUPPLEMENTARY NOTES
MIPR 11621803, DCS G9

14. ABSTRACT
Visual inspection is the most used method to detect seepage at dams. Early detection can be difficult with this method, and use of appropriate real time monitoring could significantly increase the chances of recognizing possible failure. Seepages can be identified by analyzing changes in water and soil temperature. Optical fiber placed at the embankment's downstream toe has been proven to be an efficient means of detecting real time changes at short intervals over several kilometers. This study aims to demonstrate how temperatures measured using fiber optic distributed sensing can be used to monitor seepage at Moose Creek Dam, North Pole, Alaska. The fiber optic cable portion of the monitoring system is installed along a section of the embankment where sand boils have occurred. Though no flood event occurred during this monitoring period, routine pumping tests of nearby relief wells resulted in an increase of soil and water temperature (up to 13°C) along a 100 m section where sand boils were detected during the 2014 flood events. Measurements during a flood event are expected to provide a quantitative assessment of seepage and its rate.

15. SUBJECT TERMS
Arctic watershed; HEC; Runoff; Snow water equivalent; Snowmelt; Stage-frequency curves; Utqiaġvik

16. SECURITY CLASSIFICATION OF:			17. LIMITATION OF ABSTRACT SAR	18. NUMBER OF PAGES 62
a. REPORT Unclassified	**b. ABSTRACT** Unclassified	**C. THIS PAGE** Unclassified		

19a. NAME OF RESPONSIBLE PERSON Anna M. Wagner	19b. TELEPHONE NUMBER (include area code) (907) 361-5459

STANDARD FORM 298 (REV. 5/2020)
PREVIOUS EDITION IS OBSOLETE.
Prescribed by ANSI Std. Z39.18

7. PERFORMING ORGANIZATION NAME(S) AND ADDRESS(ES) (concluded)
US Army Engineer Research and Development Center (ERDC)
Cold Regions Research and Engineering Laboratory (CRREL)
72 Lyme Road
Hanover, NH 03755-1290

Silixa LLC
3102 W Broadway Street
Missoula, MT 59808

HydroResearch AB
Stora Marknadsvägen 15, 12th floor
SE-183 34 Täby
Sweden